



AFRL-AFOSR-UK-TR-2011-0061



Starting Processes of High Contraction Ratio Scramjet Inlets

Alex Grainger
Guillermo Paniagua

Institut von Karman de Dynamique des Fluides
Waterloosesteenweg 72
Rhode-St-Genèse, Belgium 1640

EOARD Grant 10-3059

Report Date: January 2012

Final Report from 23 June 2010 to 23 June 2011

Distribution Statement A: Approved for public release distribution is unlimited.

Air Force Research Laboratory
Air Force Office of Scientific Research
European Office of Aerospace Research and Development
Unit 4515 Box 14, APO AE 09421

REPORT DOCUMENTATION PAGE

Form Approved OMB No. 0704-0188

Public reporting burden for this collection of information is estimated to average 1 hour per response, including the time for reviewing instructions, searching existing data sources, gathering and maintaining the data needed, and completing and reviewing the collection of information. Send comments regarding this burden estimate or any other aspect of this collection of information, including suggestions for reducing the burden, to Department of Defense, Washington Headquarters Services, Directorate for Information Operations and Reports (0704-0188), 1215 Jefferson Davis Highway, Suite 1204, Arlington, VA 22202-4302. Respondents should be aware that notwithstanding any other provision of law, no person shall be subject to any penalty for failing to comply with a collection of information if it does not display a currently valid OMB control number.

PLEASE DO NOT RETURN YOUR FORM TO THE ABOVE ADDRESS.

1. REPORT DATE (DD-MM-YYYY) 23-01-2012			2. REPORT TYPE Final Report		3. DATES COVERED (From – To) 23 June 2010 – 23 June 2011	
4. TITLE AND SUBTITLE Starting Processes of High Contraction Ratio Scramjet Inlets			5a. CONTRACT NUMBER FA8655-10-1-3059 5b. GRANT NUMBER Grant 10-3059 5c. PROGRAM ELEMENT NUMBER			
6. AUTHOR(S) Alex Grainger Guillermo Paniagua			5d. PROJECT NUMBER 5e. TASK NUMBER 5e. WORK UNIT NUMBER			
7. PERFORMING ORGANIZATION NAME(S) AND ADDRESS(ES) Institut von Karman de Dynamique des Fluides Waterloosesteenweg 72 Rhode-St-Genèse, Belgium 1640			8. PERFORMING ORGANIZATION REPORT NUMBER N/A			
9. SPONSORING/MONITORING AGENCY NAME(S) AND ADDRESS(ES) EOARD Unit 4515 BOX 14 APO AE 09421			10. SPONSOR/MONITOR'S ACRONYM(S) AFRL/AFOSR/RSW (EOARD)			
			11. SPONSOR/MONITOR'S REPORT NUMBER(S) AFRL-AFOSR-UK-TR-2011-0061			
12. DISTRIBUTION/AVAILABILITY STATEMENT Approved for public release; distribution is unlimited. (approval given by local Public Affairs Office)						
13. SUPPLEMENTARY NOTES						
14. ABSTRACT <p>An experimental campaign was undertaken at the Von Karman Institute, Belgium, aimed at investigating the sliding doors inlet starting mechanism for a hypersonic scramjet inlet. This campaign provides the first step upon a much larger inlet starting investigation, with the results providing a backbone for comparison to future 2D and 3D transient RANS numerical studies. A scaled 2D representation of the SCRAMSPACE-I geometry was constructed, with two steel 3.2mm thick doors extending upstream from the inlet leading edge at an angle of 20 degrees. After achieving steady flow conditions, the doors were then retracted via a pneumatic piston and cabling system, with the resulting flow phenomena captured via visualization as well as quantitative instrumentation. The test campaign was undertaken in the H3 Wind Tunnel Facility, which provided a jet at Mach 6 at various reservoir pressures, with variance in Reynolds number used to simulate changing altitude conditions. Due to limitations with regards to tunnel blockage and diffuser placement, a scaling factor of 5.1 was applied to the model geometry proportionally in both the x and y directions. Successful inlet starting was achieved at conditions simulating flight at an altitude of approximately 29 km. Schlieren visualization techniques were employed, showing that supersonic conditions were indeed obtained in the inlet for approximately 32 flow lengths. Senflex thin film arrays, located on the inner surfaces of the inlet, captured the transient heat flux progression at different locations along the inlet. These profiles accurately captured the phenomena observed via the Schlieren imaging, in particular the propagation of shock structures into the inlet during the inlet starting procedure. Stanton number distributions along both arrays were extracted and showed a close comparison to those expected from numerical simulations reconstructed test flow conditions, which lends credibility to the integrity of the heat flux results. Additional pressure measurements were taken, with 8 Entran EPIH-11 sensors mounted flush with the inlet internal. The pressure profiles were captured, however due to apparent calibration errors the true measured pressure magnitude in terms of Pascals was not captured. That said the data can indeed be used to compare to future numerical simulations via amplitude scaling.</p>						
15. SUBJECT TERMS EOARD, Scramjet Technology, Hypersonics, Airbreathing Engines						
16. SECURITY CLASSIFICATION OF: a. REPORT UNCLAS		17. LIMITATION OF ABSTRACT b. ABSTRACT UNCLAS c. THIS PAGE UNCLAS SAR		18. NUMBER OF PAGES 43	19a. NAME OF RESPONSIBLE PERSON Gregg Abate 19b. TELEPHONE NUMBER (Include area code) +44 (0)1895 616021	

1.0 Abstract

An experimental campaign was undertaken at the Von Karman Institute, Belgium, aimed at investigating the sliding doors inlet starting mechanism for a hypersonic scramjet inlet. This campaign provides the first step upon a much larger inlet starting investigation, with the results providing a backbone for comparison to future 2D and 3D transient RANS numerical studies. A scaled 2D representation of the SCRAMSPACE-I geometry was constructed, with two steel 3.2mm thick doors extending upstream from the inlet leading edge at an angle of 20 degrees. After achieving steady flow conditions, the doors were then retracted via a pneumatic piston and cabling system, with the resulting flow phenomena captured via visualisation as well as quantitative instrumentation.

The test campaign was undertaken in the H3 Wind Tunnel Facility, which provided a jet at Mach 6 at various reservoir pressures, with variance in Reynolds number used to simulate changing altitude conditions. Due to limitations with regards to tunnel blockage and diffuser placement, a scaling factor of 5.1 was applied to the model geometry proportionally in both the x and y directions. Successful inlet starting was achieved at conditions simulating flight at an altitude of approximately 29 km. Schlieren visualisation techniques were employed, showing that supersonic conditions were indeed obtained in the inlet for approximately 32 flow lengths. Senflex thin film arrays, located on the inner surfaces of the inlet, captured the transient heat flux progression at different locations along the inlet. These profiles accurately captured the phenomena observed via the Schlieren imaging, in particular the propagation of shock structures into the inlet during the inlet starting procedure. Stanton number distributions along both arrays were extracted and showed a close comparison to those expected from numerical simulations reconstructed test flow conditions, which lends credibility to the integrity of the heat flux results. Additional pressure measurements were taken, with 8 Entran EPIH-11 sensors mounted flush with the inlet internal. The pressure profiles were captured, however due to apparent calibration errors the true measured pressure magnitude in terms of Pascals was not captured. That said the data can indeed be used to compare to future numerical simulations via amplitude scaling.

Table of Contents

1.0	Abstract	2
2.0	Introduction.....	5
3.0	Experimental Facility and Institute Overview	6
4.0	Experimental Design.....	7
4.1	Test Conditions and Inlet Geometry	7
4.2	Experimental Model Design	9
4.2.1	Initial Flexible Sliding Door Design	9
4.2.2	Rigid Sliding Door Design.....	10
4.2.3	Sliding Door Geometry	11
4.2.4	Actuation Design.....	12
4.3	Instrumentation and Data Acquisition	16
4.3.1	Thin film Gauges	16
	To resolve the heat flux to the surface of the model from these results, the classical one-dimensional unsteady conduction equation is solved via numerical methods:	18
4.3.2	Pressure Transducers.....	19
4.3.3	Schlieren Techniques	20
5.0	Results.....	21
5.1	Schlieren Results.....	21
5.2	Heat Flux Results	24
5.2	Pressure Results	31
6.0	Discussion and Sources of Error	34
7.0	Future Activities.....	37
8.0	Conclusions.....	38
9.0	Bibliography	39
	Appendix A – Calibration Curves.....	40
	Appendix B – Design Information.....	42

Nomenclature

A^* – inlet throat area

A_i – inlet entrance area

∞ – freestream conditions

M – Mach number

t – time unless otherwise stated

x, y – cartesian coordinate system

T – temperature

P – pressure

u – flow velocity (x component)

Re – Reynolds number

E – raw signal amplitude in volts

α – thermal diffusivity

Q – heat flux

w – wall conditions

K – thermal conductance

η – stability factor

Note: for this report, thin film instrumentation elements are labelled as $*/**$, where * denotes which inlet geometry section the sensor is mounted upon (1 for bottom, 2 for top) and ** denotes the sensor element #. In this case the element # starts at one and increases as the mounting location approaches the combustor. Pressures transducer elements are numbered 1 through to 8, with 1-4 located on the bottom section. Sensors 5-8 are the top inlet sections equivalents of sensors 1-4 (i.e. sensor 1 mounted at the same x location as sensor 5)

2.0 Introduction

Achieving a started inlet flow regime is a critical design issue with regards to practical scramjet flight, as supersonic flow conditions in the combustor are a necessary component of successful hypersonic flight^{1, 2}. The “inlet starting problem” is essentially one of managing the inlet starting needs of the flight vehicle with a desire for higher local pressures in the combustor, which are generated by flow compression via the contracting nature of the inlet geometry. For practical scramjet flight, rarely will an inlet geometry be used such that it is located in the upper spontaneous starting region of Fig. 1, representing conditions for which the Kantrowitz self-starting criterion has been satisfied. In this case supersonic conditions will be present in the combustor, commonly referred to as “started flow”. While started flow will be ensured at these conditions, lower pressures will be recovered at the combustor entrance resulting in lower combustor efficiency. Alternatively if the inlet geometry is over contracted such that the inlet lies below the blue isentrope line on Fig. 1, started flow is not possible at any stage², resulting in a lack of thrust production that can lead to terminal flight failure. Between these two regions however lie conditions of great interest. Both started and unstated solutions are possible for an inlet located in this region, meaning that it is possible to utilise high contraction ratio inlets during flight, so long as started flow is guaranteed by some artificial means.

Current design practice typically involves combining classical Kantrowitz theorem in conjunction with variable inlet geometry techniques^{3, 4}. If the inlet geometry is temporarily manipulated for a given freestream Mach number such that the effective contraction of the inlet is temporarily reduced, Kantrowitz theorem dictates that the inlet will undergo spontaneous starting (i.e. pushing upwards in the y direction on Fig. 1). With a started flow regime ensured, the inlet can revert back to the original, higher contraction geometry configuration, with steady operation possible from this point onwards. (Note: green dot on Fig. 1 represents typical scramjet inlet geometry)

The *sliding doors inlet starting mechanism* is one such technique which utilises this methodology. This method consists of two doors protruding upstream from the leading edge of the inlet geometry at a designated angle (usually between 20 and 40 degrees), ensuring an initial attached oblique shock is present at the leading edge of the doors. This shock structure is significantly weaker than the detached bow shock synonymous with unstated flow regimes, which allows for started flow to be more easily achieved. The doors are then retracted up into/over the scramjet geometry causing a more gradual increase in the inlet’s effective contraction ratio.

Previously this method of inlet starting has been investigated numerically³ in 2D axisymmetric space (Mach 8) at an altitude of 30 km using Reynolds-averaged time accurate techniques, with Mach contour snapshots at various global time steps outlined on Fig. 2. In this case, the sliding doors are retracted up into the scramjet body, over a time period of 50ms. A jet forms at the centre line, with the initial subsonic internal flow prior to opening being swept into the combustor by the propagation

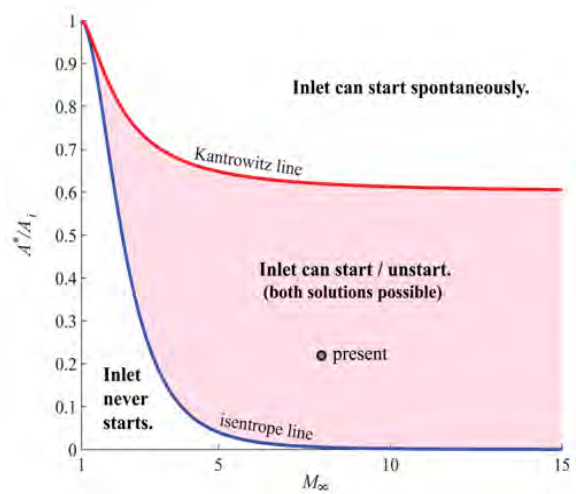


Figure 1: Families of possible inlet starting solutions, governed via Kantrowitz theorem²

of shock structures. However, while this technique shows promise, it is important to undertake an experimental analysis of this technique as a means of validating this theory. As such an experimental campaign was undertaken at the Von Karman Institute for Fluid Dynamics, making use of the H3 blow-down wind tunnel facility. The key objectives here were to:

- Experimentally investigate the applicability of the sliding doors mechanism towards successfully ensuring started flow for high contraction ratio inlets
- Obtain quantitative data which can be used for code verification in numerical reconstruction of the experimental campaign
- Visualise the flowfield during the inlet starting procedure, to compare to previous numerical sliding door results
- Identify key flow structures present during the inlet starting procedure which hamper the inlet starting process

3.0 Experimental Facility and Institute Overview

The Von Karman Institute is a non-profit, NATO funded facility located just outside Brussels, Belgium, specialising in fluid dynamics research with approximately 50 different wind tunnels, turbomachinery and other experimental facilities on site. In particular, the institute boasts a 1200 KW induction plasmatron, the most powerful induction-coupled plasma tunnel in the world. This experimental campaign however was undertaken in the H3 wind tunnel facility schematically outlined on Fig. 3.

The H3 facility is a blow down high enthalpy facility with the reservoir heated via a pebble bed heater which provides pressures ranging from 10 to 31 bar. During testing the fast acting valve is opened and the air expands through the nozzle and into the test section at a constant Mach number of 6. The flow then passes out past the test section, through the diffuser and into the supersonic ejector. The most desirable attribute of this facility is that it can provide test times of up to 20 seconds, making it ideal for inlet starting experimental studies. However this facility is sensitive to blockage⁵ and as such limiting the model cross-sectional size was a primary concern when designing the experimental model.

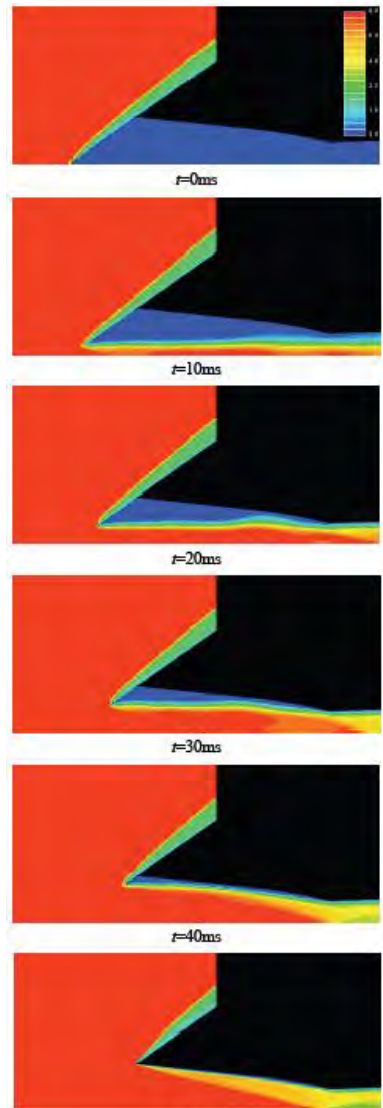


Figure 2: Transient Mach snapshots (range 0-8)

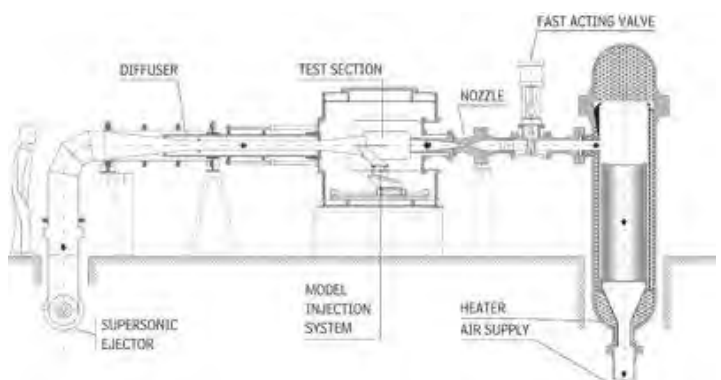


Figure 3: H3 Wind Tunnel Facility Schematic

4.0 Experimental Design

Several key components had to be considered in accordance with the objectives of the overall experimental campaign. The final model design must accommodate the mounting of the experimental instrumentation such that accurate quantification of the flow during door motion can be achieved. Additionally an actuation mechanism needed to be implemented such that it could both slide and guide the doors without adversely affecting normal operation of the facility. However the first consideration to be made was to ensure that the inlet geometry lies within the dual solution region of Fig. 1 and that the freestream conditions provided by the wind tunnel facility are comparable to those experienced during practical flight.

4.1 Test Conditions and Inlet Geometry

The experimental model cross-sectional geometry is a scaled 2D equivalent representation of the SCRAMSPACE-I inlet. The cross-sectional features are outlined below on Fig. 4. The main features of the inlet geometry are as follows:

- single ramp inlet contraction
- 0.5 mm radius leading edge
- Contraction Ratio (CR) of approximately 2.1
- Inlet length of 0.06m (x direction), measured from leading edge tip to inlet's end

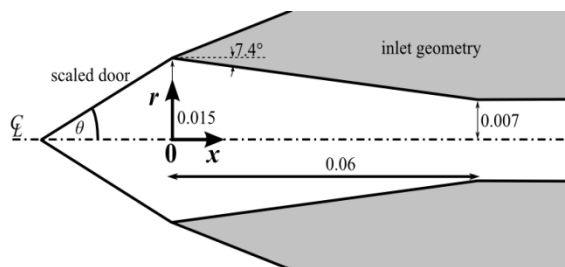


Figure 4: Experimental Inlet Geometry

A single ramp was chosen for this experimental setup as it was decided that the investigation should start at the lowest level of complexity. Additionally a reference length of 0.06m (scaled down from a full sized inlet of approximately 0.31 m) was chosen such that the experimental conditions present in the test facility would be comparable to those experienced during flight, while still providing a model geometry which can be used safely within the H3 wind tunnel (verified by preliminary blockage test results). A scaling factor of approximately 5.1 was applied such that the inlet remained proportionally identical to a scaled 2D representation of the SCRAMSPACE-I inlet, excluding certain dimensions which will be outlined in following sections.

Fig. 5 outlines the SCRAMSPACE-I trajectory, plotting altitude versus $Re_x = 0.06m$, where the yellow region represents the fuel on phase of the flight experiment. Using the reference length of 0.06m, the green dots represent conditions that the model will experience at 10, 20 and 30 bar respectively in the H3 Wind Tunnel Facility.

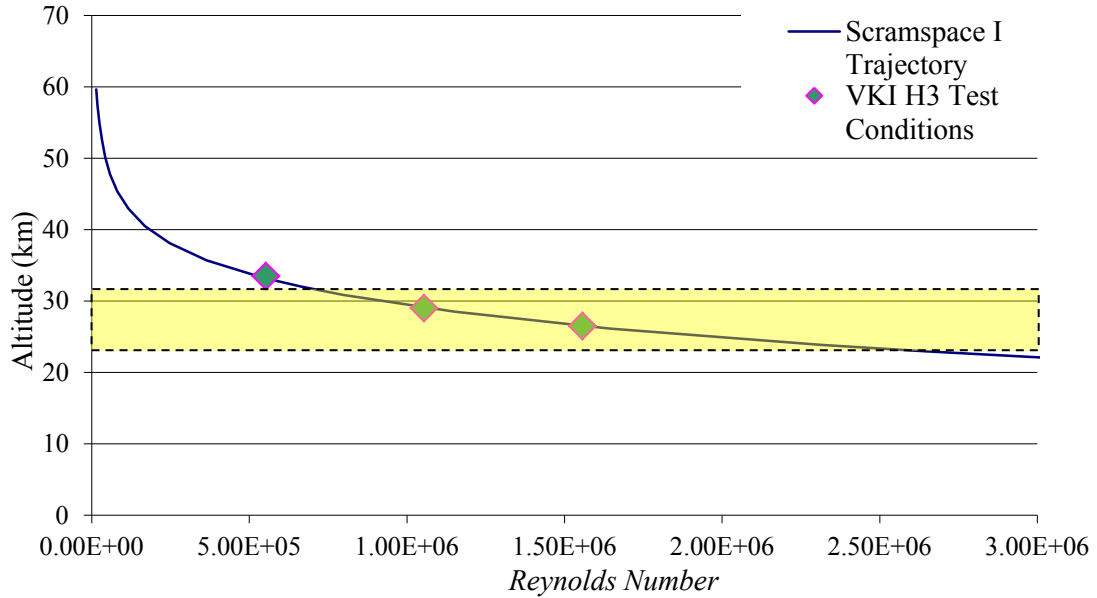


Figure 5: Comparison of experimental conditions to a practical scramjet flight trajectory

The experimental conditions are above shown to match well with the trajectory curve and in particular are close to the fuel on segment of the trajectory. This is ideal as ensuring a started flow regime in this region is critical for practical scramjet flight. As such it was initially proposed that the experimental conditions shown on Fig. 5 form the basis of this experimental investigation. These experimental conditions are shown quantitatively below:

P0(Pa)	T0(K)	T(K)	P(Pa)	u(m/s)	Re _x	Altitude (km)
3.0E+06	500	61	1963	939	1.6E+06	26.5
2.0E+06	500	61	1330	939	1.1E+06	29
1.0E+06	500	61	697	939	5.5E+05	33.5

Table 1: H3 Experimental Conditions

The basis for the experimental geometry as mentioned was the SCRAMSPACE-I inlet geometry which has a contraction ratio of approximately 4.8. In this case the inlet geometry is axisymmetric rather than 2D and therefore the inlet ramp angle has been changed from the original angle of 5.7 degrees (applicable to the first inward turning ramp of SCRAMSPACE-I) as the cross-sectional area is now a function of the inlet vertical height D (m), rather than radius squared (m²).

While the model was proportionally scaled, the leading edge of the inlet could not be scaled relative to the reference length of 0.06m due to practical machining considerations. This in addition to the shorter inlet length of the experimental model caused the leading edge shock angle to impinge much further upstream of the throat after reflecting off the centreline, as per Fig. 6. This change in shock impingement ultimately results in an unstarted solution, due to a separated region forming downstream of the shock impingement and ultimately choking the internal flowfield.

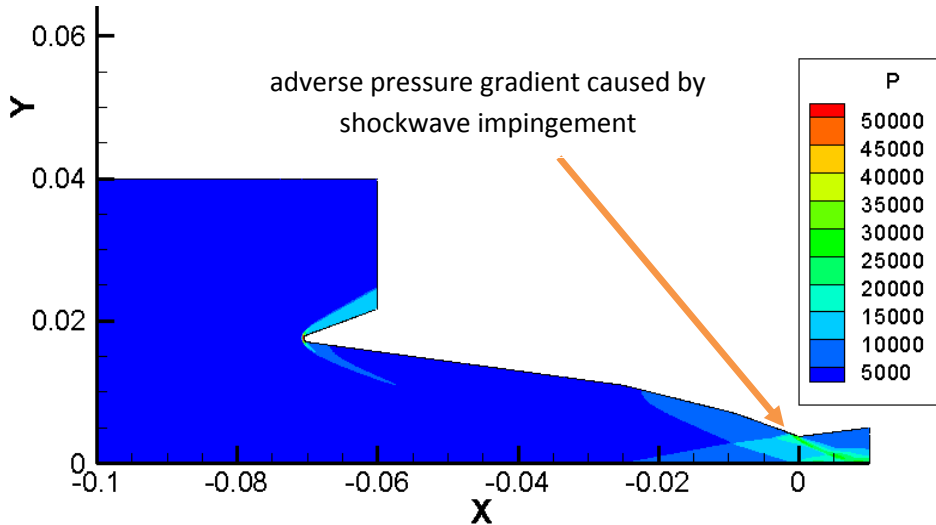


Figure 6: Pressure contours showing region of separation caused by the retention of the 0.5mm leading edge (Note: In this case, a slightly longer reference has been used, as these computations were undertaken prior to the original blockage tests used to determine the reference length of 0.06m)

As a result the throat sizing was increased to 14 mm as per Fig. 4 to ensure that the leading edge shock impinged downstream of the inlet throat. This resulted in the inlet geometry providing a contraction ratio of approximately 2.1, with the inlet remaining in the dual solution region of Fig. 1.

With the internal geometry of the inlet now determined and verified to fit into the H3 wind tunnel without causing tunnel blockage, the major mechanical components of the experimental model, namely the design of the actuation device, could then be implemented.

4.2 Experimental Model Design

4.2.1 Initial Flexible Sliding Door Design

It was proposed that the sliding door would be a single flexible piece with a sharp leading edge, with the door motion controlled by sliding the door inside grooves in the side walls of the model, such that the door movement resembled a “garage door” like process. The path would curve along the inner side plates of the model, over the leading edge region of the model, then track straight downstream from then onwards as per Fig. 7. In this case the door would bend during the inlet starting procedure, requiring the material to be flexible in the downstream direction yet be rigid in the lateral direction, such that the door does not deform due to forces imposed by the flow prior to retraction. It was initially proposed that a carbon fibre piece coupled with an additional heat shield be used, however due to procurement difficulties this design was not possible, ultimately leading to the discontinuing of the flexible door proposal. This ultimately led to the final rigid sliding door design, which was used as part of the experimental campaign.

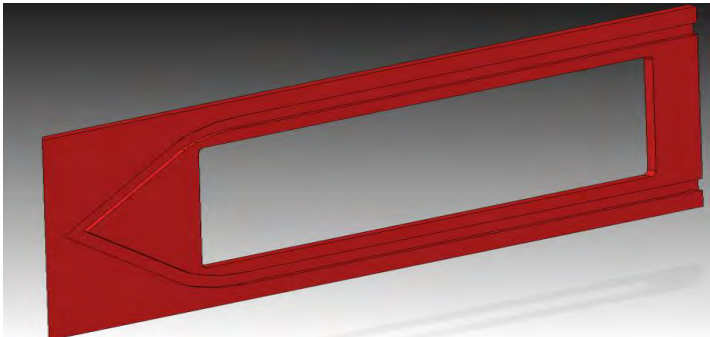


Figure 7: Initial concept, with grooves carved into the side plates serving as the guidance mechanism

4.2.2 Rigid Sliding Door Design

Instead of employing a flexible door, it was proposed that a simplified rigid door be used. Additional modifications in the way that doors would be guided were needed, namely a supplementary component to the side door groove to control the doors motion. To achieve this the experimental sliding door is guided via a coupled “pin and slot” guidance system. A 2mm pin mounted into the sliding door slides along a horizontal groove in the side plate (primary groove), as per Fig. 8. An additional secondary groove is cut into the side of the sliding door, with an extra fixed pin from the side plate controlling the vertical component of the door motion. By controlling the profile of the primary groove and ensuring that the pin from the side plate (sliding inside the secondary groove) is stationary, the motion of the door can be predetermined and controlled.

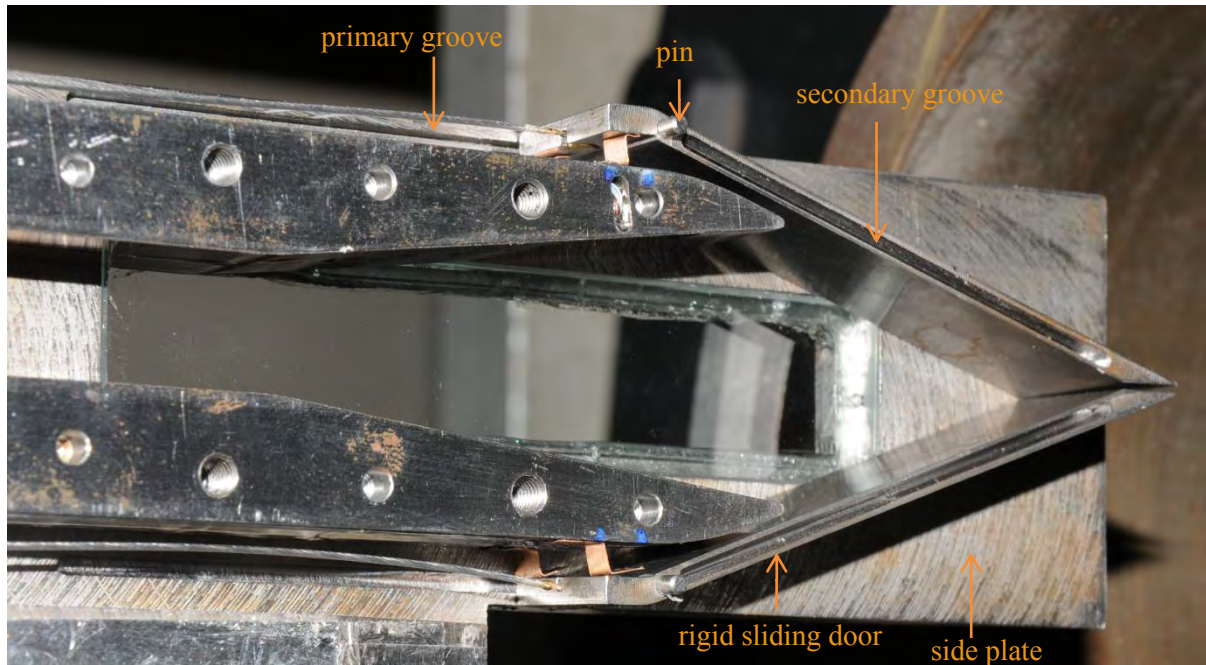


Figure 8: Experimental Model Cross-section, with important features highlighted

As a result of this the motion of the sliding door has changed from what was previously numerically investigated, with the door motion now incorporating a rotational component rather than being strictly translational. A schematic outline of the motion of the door is shown on Fig. 9, with the red outline representing the final retracted position of the sliding door. It should be noted that the “S bend” copper pieces on Fig. 8 are present purely to stop the doors from opening prematurely, by imparting a resultant force on the door, acting about the pins.

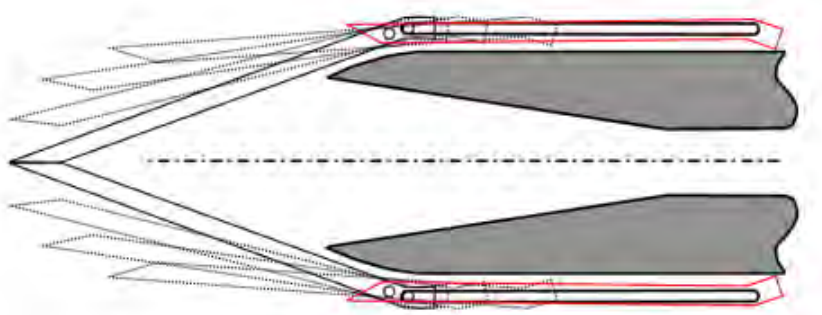


Figure 9: Motion of the rigid door at different stages of the retraction

4.2.3 Sliding Door Geometry

The sliding doors were 3.2 mm thick mild steel pieces, which when joined together form a sharp leading edge at the foremost upwind point. As mentioned previously it is important for this method of inlet starting to ensure an attached oblique shock at the leading edge prior to opening. As such a door inclination angle of 20 degrees was chosen to ensure that this condition is reached for all tunnel test conditions. Additional sliding door geometry can be seen on Fig. 10.

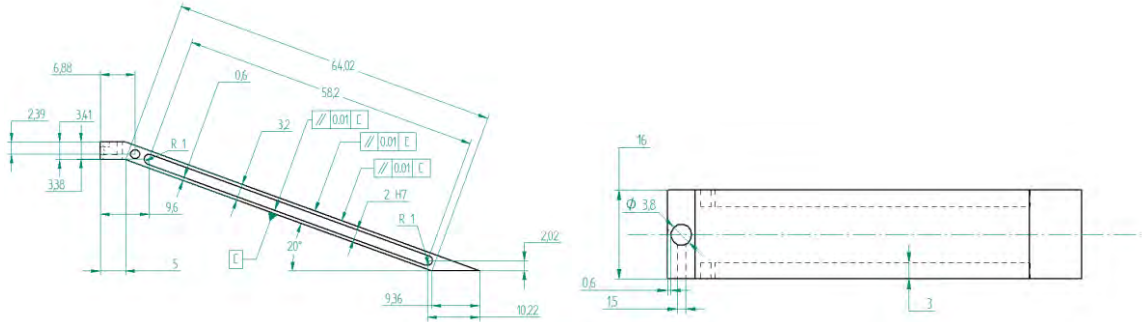


Figure 10: Sliding door CAD drawing, showing major dimensions

A coarse FEA validation of the chosen thickness was undertaken to investigate whether standard alloy steel would be sufficient to maintain the door's structure prior to opening the doors from their initial retracted state. Fixed boundary conditions were applied for the pin surfaces and at the interface between the two doors. The calculation in this case applied the force imposed by the stagnation pressure along the entirety of the outer surface, normal to the surface. The von Mises stress and displacement results are shown on Figs. 11 and 12, where it can be seen that the maximum stress values are well below acceptable suitable safety margins when employing steel as the door material.

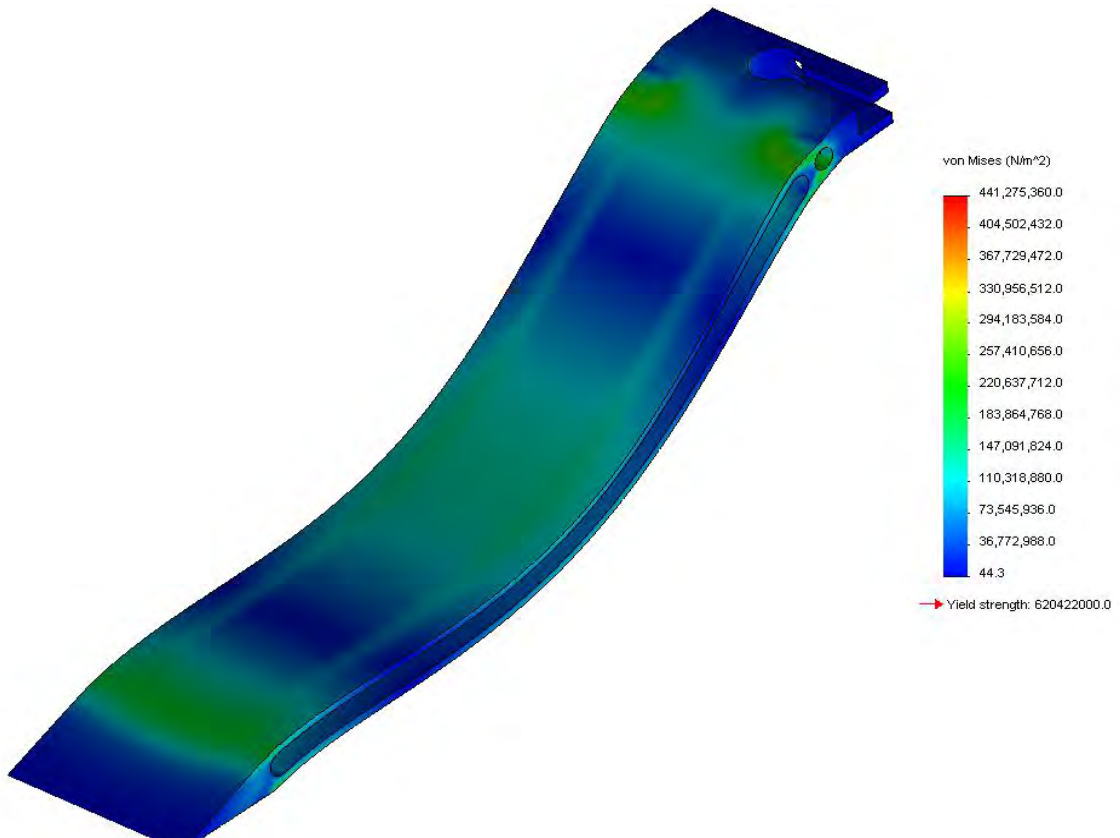


Figure 11: FEA Von Mises stress results, showing maximum stress is well below yield, even when applying the stagnation pressure along the entire surface

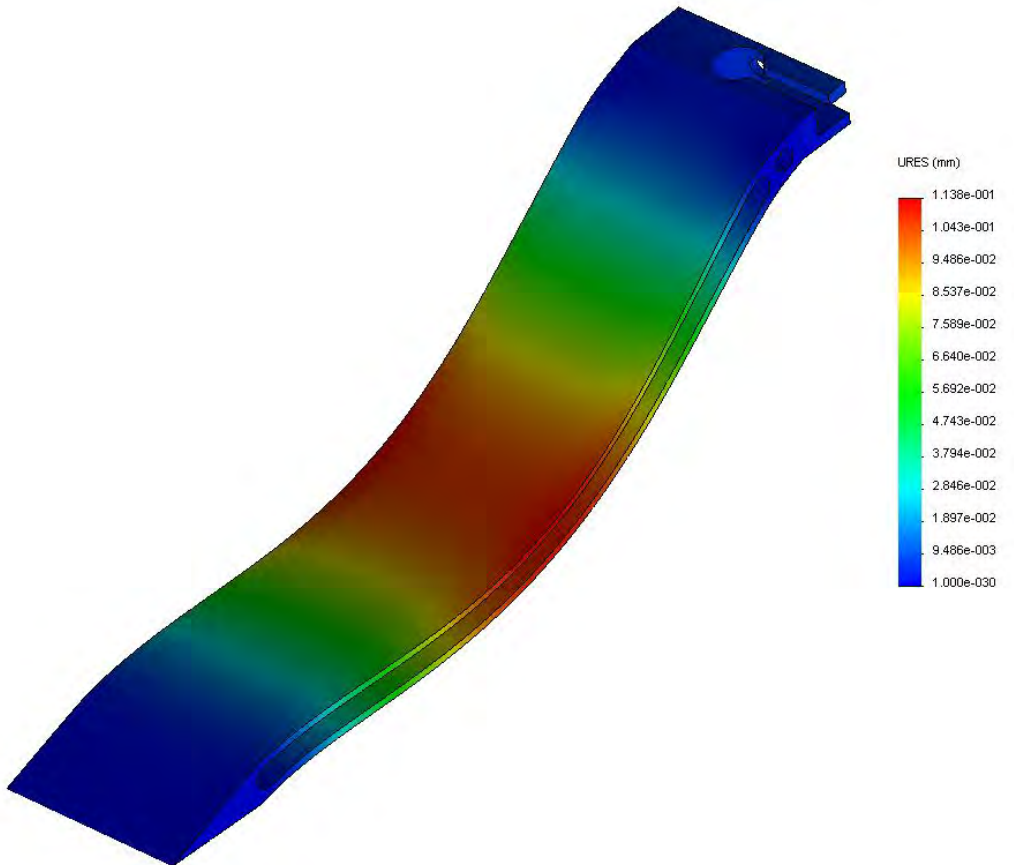


Figure 12: URES displacement results for the sliding door, when experiencing the stagnation pressure along the entire outer surface prior to opening

4.2.4 Actuation Design

The initial design for the experimental sliding door actuation is outlined below on Fig. 13. The doors would be actuated via two pneumatic pistons, one for each of the sliding doors, connected to the doors via a cabling system. These pistons would then be mounted inside the model geometry, actuating through the central plane of the doors for greater control. However such a piston would need to be of a non-realistic size if it were to be stored internally inside the model. Additionally it is preferable to control the motion of the doors via one pneumatic piston, thereby coupling the motion during retraction.

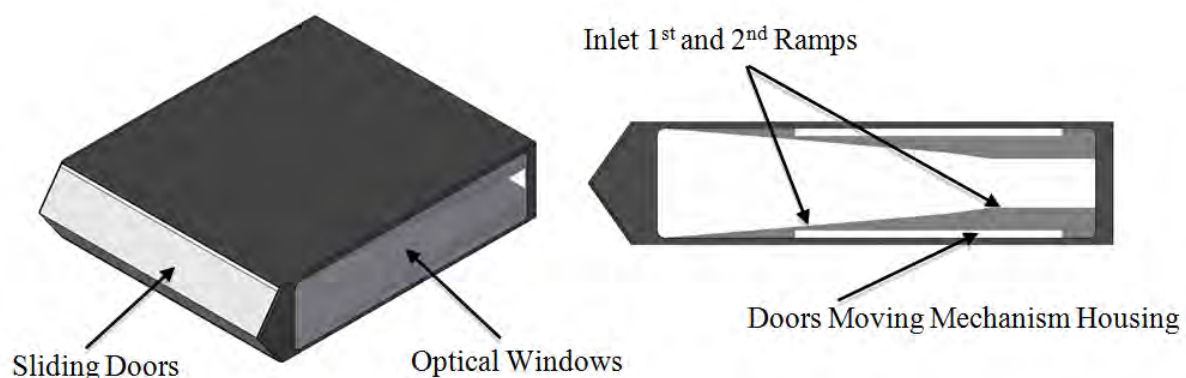


Figure 13: Initial Door Actuation Concept

With these issues in mind, a single piston mounted externally to the inlet geometry was determined to be the best solution. The piston model chosen would have to have the following specifications:

- maximum stroke equal to or greater than 60mm (distance to fully retract the sliding doors from origin)
- impart a retraction force such that the doors are opened quickly (order of 10ms)
- require reasonable operating pressures (≈ 5 bar pressure)
- be of a cross-sectional size such that it can fit successfully inside the H3 wind tunnel

The Martonair model M/548, 100mm stroke pneumatic piston was selected in accordance with these requirements. The primary dimensions are outlined below on Fig. 14, with Fig. 15 outlining the forces provided at various air supply pressures (Note: *Force tige rentrante en N* translates to the piston retraction force in N).

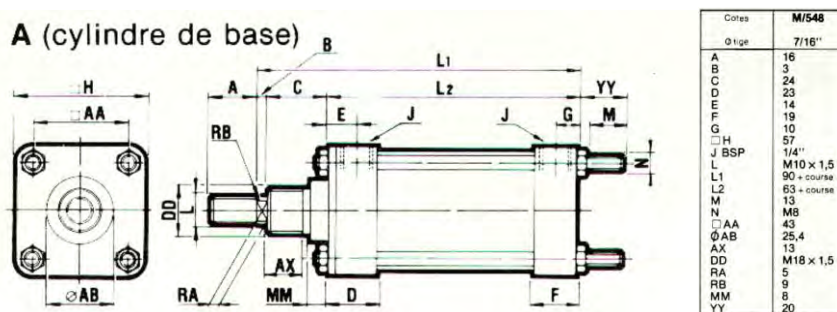


Figure 14: Martonair M/548 piston dimensions

Pression de service en bars		2	3	4	5	6	7	8	9	10
M/549	FORCE tige sortante en N*	158,8	238,2	317,6	397	476,4	555,8	635,2	714,6	794
	CONSOMMATION en ltr./cm. de course	0,024	0,032	0,040	0,048	0,056	0,064	0,072	0,080	0,088
	FORCE tige rentrante en N*	140,8	211,2	281,6	352	422,4	492,8	563,2	633,6	704
M/548	FORCE tige sortante en N*	311	466,5	622	777,5	933	1088,5	1244	1399,5	1555
	CONSOMMATION en ltr./cm. de course	0,047	0,062	0,078	0,093	0,109	0,124	0,140	0,155	0,171
	FORCE tige rentrante en N*	291,8	437,7	583,6	729,5	875,4	1021,3	1167,2	1313,1	1459
M/547	FORCE tige sortante en N*	633,2	949,8	1266,4	1583	1899,3	2216,2	2532,8	2849,4	3166
	CONSOMMATION en ltr./cm. de course	0,095	0,127	0,158	0,190	0,221	0,253	0,285	0,316	0,348
	FORCE tige rentrante en N*	593,6	890,4	1187,2	1484	1780,8	2077,6	2374,4	2671,2	2968

Figure 15: Martonair pneumatic piston specifications, with the specifications relevant to the experimental campaign highlighted

The procedure used for the H3 wind tunnel during operation involves injecting the model into the flow via the primary piston shown on Fig. 16 after steady flow conditions have been established in the test chamber. It was therefore proposed that the pneumatic piston driving the sliding door motion be mounted such that it too is injected at the same time as the inlet geometry, to avoid unnecessary complications with regards to cable pathing after model injection. To accommodate this a new model base plate was machined, such that it now extended further downstream onto which the Martonair piston could now be mounted. Two L shape steel pieces were machined to hold the piston in place, which were subsequently bolted onto the extended base plate.



Figure 16: Back end of experimental test chamber, showing the coupling of the pneumatic piston to the experimental model for injection purposes

Additionally a method of ensuring proper interaction between the piston and the doors is required. The simplest means of achieving this was via a cabling system, using a steel nylon coated cable of 0.7mm diameter. A brass cylindrical attachment was screwed onto the piston con-rod, with a brass champignon/mushroom connector sliding into a slot cut-out on the model side of the cylinder, as per Fig. 17. Two holes have been drilled through the champignon to allow the two cables to pass through, fixed by passing the ends through a small piece of steel tubing and then clamping down to fix the cables inside as per Fig. 17.

As the maximum stroke of the piston is significantly longer than the pathing of the sliding door grooves (approximately 58mm), breaking of the cabling system at the end of the sliding doors' motion was a concern. As per Fig. 15 an Aluminium "stopper" cylinder was screwed onto the front side of the piston, such that the con-rod can slide without hindrance through the stopper. However when the brass cylindrical piece shown on Fig. 17 hits the aluminium stopper, further motion of the piston is now impossible, allowing any excessive strain on the cabling to be avoided.

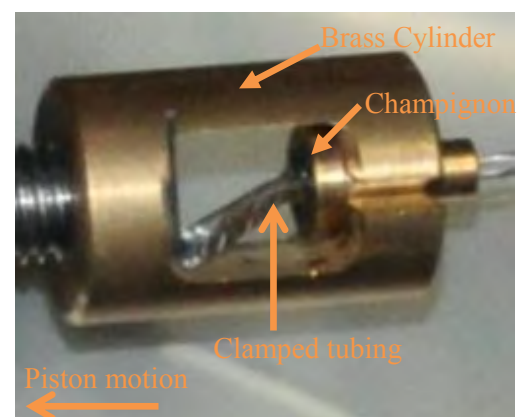


Figure 17: Piston side connector, showing interface between door cabling and the piston con-rod

On Fig. 8 it can be seen that at the downwind end of the sliding door, a flat region protrudes out from the inclined surface parallel to the flow. The cable was attached at this point, with each cable soldered to a simple brass cylindrical attachment of 3.8mm diameter, which was then popped into a hole drilled into the flat region of each door. This is shown more clearly above on Fig. 18.



Figure 18: Underside view of the sliding door, showing the cabling attachment on this side

It was also desired that the cables' exposure to the flow be minimised, with the cables following the profile of the base and mounting system of the H3 facility, shown on Fig. 15, to allow the model geometry to shield the cables from the majority of the flow. In addition, two aluminium guidance pieces have been placed at the far downstream end of the model, one on each side of the model. These pieces ensure that the cable passes straight down the centre of the model geometry, guaranteeing that any uneven lateral movement of the doors is eliminated. Both cables then pass around a cylindrical piece which is tapped into the mounting base of the experimental model, as per Fig. 15, passing back to the brass cylindrical piston attachment. In this region, the cables are well outside the jet diameter of 15 cm. While the overall lengths of the cables in this pathing system are of differing values for each door, the overall displacements for both doors when pulled will be the same, thereby ensuring that the motion of both doors stay in proportion to one another.

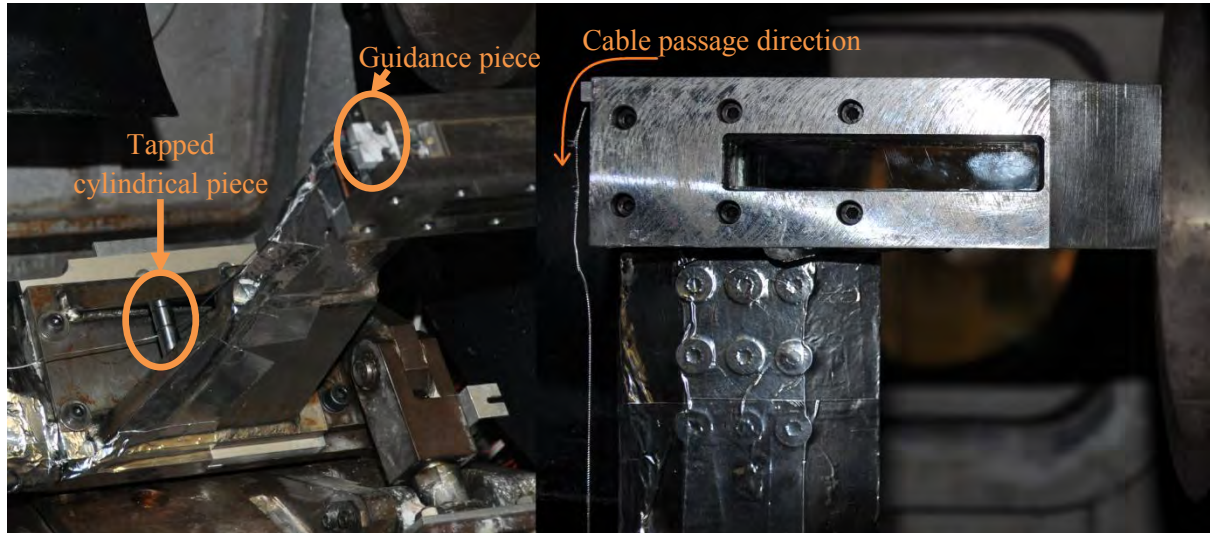


Figure 19: Passing of the cabling from the sliding doors to the piston con-rod attachment

4.3 Instrumentation and Data Acquisition

To properly extract the physical flow quantities during the inlet starting process, a number of different instrumentation types were used. Schlieren visualisation techniques have been employed, to inspect the shock profile progression during the testing period and to quickly ascertain post test whether a started solution had indeed been achieved. Additionally thin film heat transfer arrays and Entran pressure transducers have been employed to extract physical quantitative values during the inlet starting process, for comparison to past and future numerical computations.

4.3.1 Thin film Gauges

Two Senflex thin film arrays provided by Tao Systems were incorporated into the final experimental model setup and were applied along the inner surfaces of the model geometry. The second array in this case was laterally inverse to the other, such that the thin film elements on the top array were in the identical plane to those located on the bottom. Resistor elements were spaced in the x direction at increments of 14.75mm with each array consisting of eight single Nickel resistance elements which were evaporated onto a thin Upilex sheet. A schematic of the thin film array circuitry outlined on Fig. 20 and 21. Additional resistance elements were placed laterally at approximately 17.3mm downstream, to sample the 3D effects present in the inlet. Each sensor was connected to copper leads, applied to the Upilex layer, with additional holes cut into the Upilex to allow for pressure measurement readings to be conducted. The Upilex sheets were applied flush to the inner model surface, approximately 18mm downstream of the leading edge, glued with an epoxy capable of operating at Temperatures up to 120 degrees Celsius. At the trailing edge, electrical banana pin connections were soldered to the array copper leads, passing directly back to the data acquisition setup. A sampling frequency of 500 KHz was used for all tests conducted.

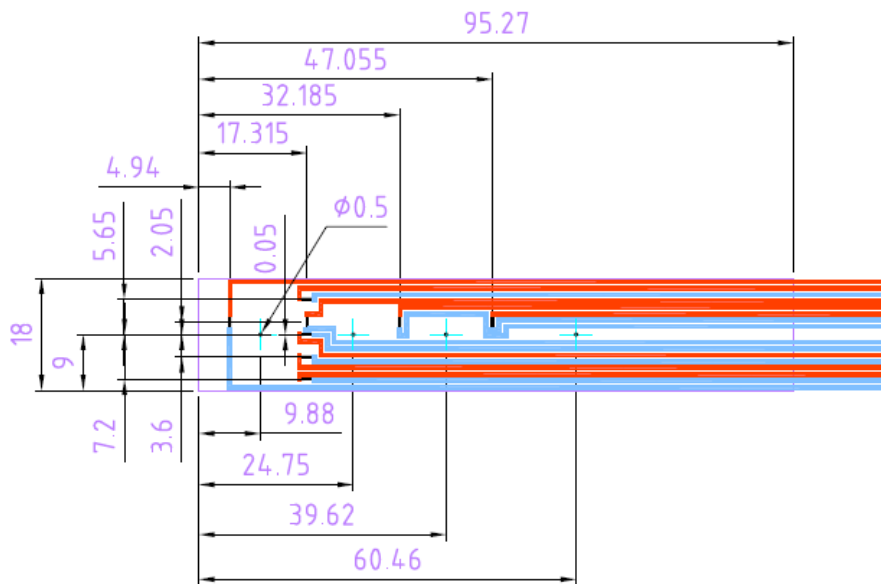


Figure 20: Schematic showing dimensional locations of thin film array elements

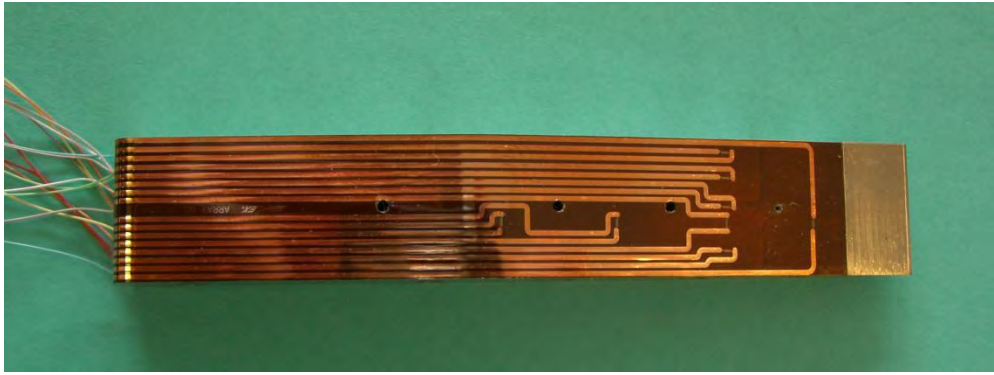


Figure 21: Senflex thin film array after being applied to the model geometry

The banana connector pins then directly passed into the “heat transfer boxes”, which contain a Wheatstone bridge operating in constant current mode from which the signal is transformed into a voltage and then recorded via the Genesis Data Acquisition System. This signal can then be converted to temperature value via extrapolation of the previously gained thin film calibration curves (see Appendix A.) To achieve this the thin film arrays were placed inside an oven operating at incrementally increasing temperature values (measured via a K-type thermocouple), with the voltage then recorded while utilising the same measurement chain as that which was used in the experimental setup.

Both heat transfer boxes can be operated in either relative or absolute resistance mode. For the relative resistance case, the signal provided is a comparison between the initial and measured signal, which is ideal for high-frequency measurements. The absolute mode output was measured and recorded shortly before injection, at which point the boxes were switched to relative mode via the “Taka Taka” box, shown on Fig. 22. This absolute mode output can therefore be used to ascertain the initial surface temperature of the model. An example of a generic voltage signal obtained via this manipulation is shown on Fig. 23. It should also be noted that the changing of the resistance mode also served as the trigger for both the high speed camera used for the Schlieren visualisation, as well as the trigger for the 32 channel data acquisition system used.

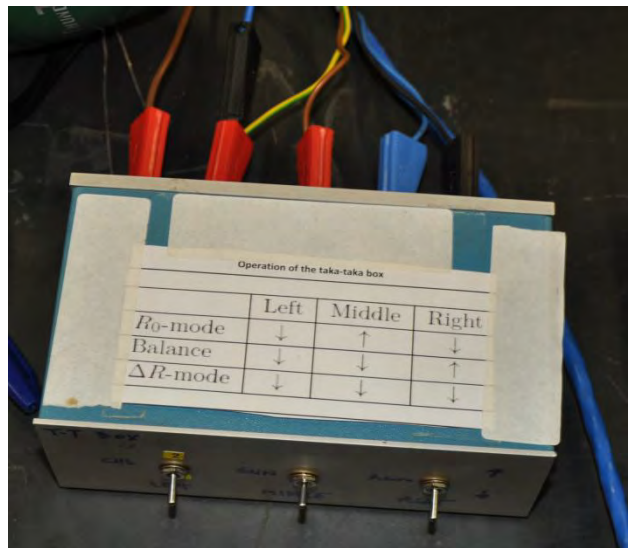


Figure 22: Taka-taka box, used to manipulate the resistance mode during testing

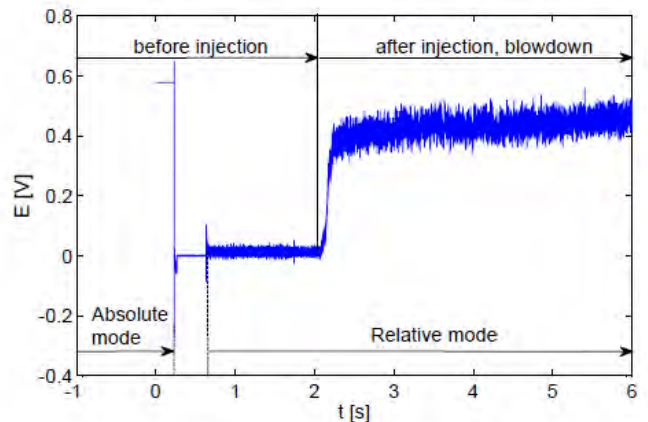


Figure 23: Typical raw thin film array signal, showing both absolute and relative resistance modes⁶

To resolve the heat flux to the surface of the model from these results, the classical one-dimensional unsteady conduction equation is solved via numerical methods:

$$\frac{\partial T(x,t)}{\partial t} = \alpha(x) \frac{\partial^2 T(x,t)}{\partial x^2}$$

Equation 1: 1D Unsteady Conduction Equation

To solve this equation certain assumptions needed to be made:

- Material properties such as thermal diffusivity, α , are assumed to be constant
- At a given substrate depth x (distance from the wall of the inlet geometry), the temperature can be considered to be constant during the short testing time (semi-infinite assumption)
- At the interface between the Upilex and the steel model, the heat flux and temperature are equal
- The initial temperature within the substrate is uniform and known (gained via the voltage signal during the absolute resistance mode prior to triggering)
- The wall heat flux is governed via Fourier's law, as per Equation 2

$$Q_w(t) = -k_1 \left(\frac{\partial T_1(t)}{\partial x} \right)_{x=0}$$

Equation 2: Fourier's Law of Heat Flux⁸

In accordance with these boundary conditions, the Crank-Nicholson scheme can be applied to Equation 1 to solve for temperature histories across the two substrates (Upilex and steel)^{6,7}. Equation 3 outlines the finite difference approach applied to solve Equation 1:

$$\frac{T_j^{m+1} - T_j^m}{\Delta t} = \eta \left[\frac{\frac{\alpha^k (T_{j+1}^{m+1} - T_j^{m+1})}{\Delta x_j} - \frac{\alpha^k (T_j^{m+1} - T_{j-1}^{m+1})}{\Delta x_{j-1}}}{\frac{\Delta x_{j-1}}{2} + \frac{\Delta x_j}{2}} \right] + (1-\eta) \left[\frac{\frac{\alpha^k (T_{j+1}^m - T_j^m)}{\Delta x_j} - \frac{\alpha^k (T_j^m - T_{j-1}^m)}{\Delta x_{j-1}}}{\frac{\Delta x_{j-1}}{2} + \frac{\Delta x_j}{2}} \right]$$

Equation 3: Crank-Nicholson Law Applied to Equation 1⁸

where k denotes the substrate material (1 or 2 for Upilex and steel respectively), j denotes the space component of the nodal point and m denotes the time superscript for each point within the substrate. η denotes the stability factor, which when greater than 0.5 ensures a decoupling of the time and space components of Equation 3. By representing the unknowns at time $m+1$ in terms of the solution at time m , a tri-diagonal system can be obtained. This system is then solved by way of a previously written FORTRAN code⁶ developed by a previous Doctoral candidate at the Von Karman Institute. From solving the above equation numerically and obtaining the 1D temperature profile at the model surface for each gauge at time $m+1$, the wall heat flux can thus be obtained via solving Fourier's Law.

4.3.2 Pressure Transducers

In addition to the Senflex heat transfer measurements, surface pressure measurements were also taken during the inlet starting procedure. Entran EPIH-11 type transducers were selected (dimensions shown on Fig. 24) due to their relatively small size and ability to provide a frequency spectrum over 100 KHz. Important technical specifications of these transducers are outlined below on Table 2. For this transducer type, a useful frequency band of 20% of the resonant is provided, in this case providing a maximum measureable frequency of 120 KHz. Additionally, an absolute pressure reference type was chosen to avoid the added complexity of including additional components for gauge/relative pressure reference transducers in the overall model geometry.

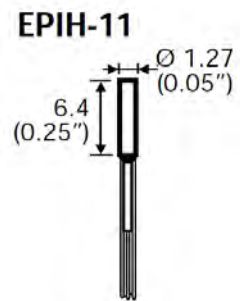


Figure 24: Entran Pressure Transducer Dimensions

Pressure Range (BAR)	Resonant Frequency	Output "FSO" nom.	Thermal Zero Shift /50°C	Operating Temperature (°C)	Pressure Reference Type
3.5	600 KHz	75 mV	± 2.5 FSO	-40 to 120	Absolute

Table 2: Entran EPIH-11 General Specifications

A total of 10 transducers were purchased with four pressure transducers planned to be mounted on each side of the inlet geometry. Fig. 25 outlines the locations and designations of the pressure transducers on the bottom geometry half. Three transducers were mounted vertically (1/2-1/4), flush with the inlet surface. A fourth was mounted horizontally near the entrance of the inlet, due to the inlet thickness at the leading edge region being smaller than the transducer length of 6.4 mm. As such, a 0.5mm hole of length 1.35 mm was drilled normal to the surface, with the transducer head screen positioned in line with the 0.5mm hole. In so doing, the signals from these pressure transducers mounted in this configuration will be delayed comparative to the flush mounted transducers. To ensure easy passage of the transducer cabling, a channel has been carved into the outer side of each inlet piece, through which the cables pass out the back of the model and into the data acquisition system.

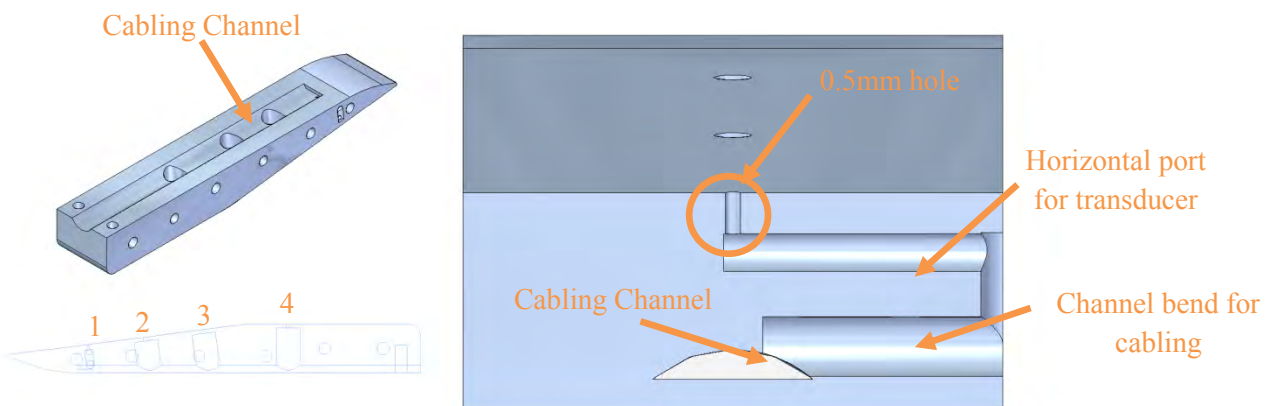


Figure 25: Transducer mounting, showing cabling channel on the upper left, transducer notation bottom left and the horizontal mounting of Transducer 1 showing modified cabling passage on the right

The pressure transducers were calibrated from vacuum conditions in the test section up until near atmospheric conditions. The calibration curves of the ten purchased pressure transducers can be found in Appendix A. By applying these calibration curves to the voltage signal gained via the data acquisition system during the inlet starting procedure, the surface pressure distribution during the inlet starting procedure can be obtained. However, while these results and the heat flux data will provide quantitative data for investigation and comparison to numerical results, visualisation techniques are also needed to better view and analyse the flow features present during inlet starting.

4.3.3 Schlieren Techniques

In addition to raw physical data, visual techniques were also employed. Schlieren imaging was used to investigate the density gradients and shock features observed during the inlet starting procedure. Conveniently a series of polished mirrors were already installed to cater for the H3 wind tunnel facility, with the mirrors able to be lowered via a mechanical pulley system. The light source in this case is provided by a light and power supply on the far side of the tunnel, operating at a constant 20V, which passes through the test chamber and to the other side. The light then reaches a converging lens, with the knife placed just prior to the lens at the focal point to cut exactly half the light spectrum. For a flow of uniform density, this will provide an image half as bright as previously seen. However during operation of the tunnel, the density variations in the flowfield will result in darker and light patches being visible, corresponding to density gradients normal to the direction of the knife. The image is then captured via the high speed camera used by experimentalists at the Von Karman Institute, capable of image processing at a frequency of up to 500 KHz. However due to onboard memory limitations and the external hard drive socket being previously broken, the maximum possible frequency for this experimental campaign was 500 Hz, limited primarily by the longer test duration needed for this experimental setup.

To visualise the flowfield inside the inlet geometry, a 95 by 21 mm cut-out has been imposed on both side plates of the model, with two 6mm thick uniform, optical quality quartz glass pieces cut to fit these regions as per Fig. 19. An in-house epoxy sealant was used instead of a typical O-ring, with both glass pieces positioned such that they are flush with the inner surface of the inlet. While basic hand calculations were undertaken to ensure that the glass was thick enough to survive the generated pressures, the model was tested at 30 bar pressure using plexiglass, to check that the 6mm thickness was sufficiently sized prior to installing the glass windows.

5.0 Results

The following results catalogue the quantitative surface results, as well as high speed Schlieren snapshots. Unfortunately a large amount of mass flow was not properly captured by the diffuser for all tests undertaken when actuating the doors, with the H3 tunnel blocking after each test regardless of whether started flow conditions for the experimental model were achieved or not. As such, the model body experienced extremely high temperatures at the end of each test, which ultimately led to the glue binding the thin film sheets to the model body beginning to fail. Ultimately this resulted in the thin film separating from the model body, leading to the premature end of the test campaign. However, successful starting of the inlet was achieved prior to this at medium Reynolds conditions (20 bar freestream total pressure), with secondary testing currently ongoing at the Von Karman Institute. As ultimately these experimental results will be used to compare and contrast with future planned numerical studies, the results included hereto in are primarily focussed upon the time domain, rather than the frequency domain.

5.1 Schlieren Results

Figs. 26 to 30 outline the experimental Schlieren results for the 20 bar experimental test, with flow passing from right to left. Fig. 26 shows the model just prior to injection into the flow ($t = 0.88$ seconds), with the main optical features labelled. Approximately 0.11 seconds after initial injection, the initial steady flowfield conditions required prior to opening the doors are achieved, as outlined on Fig. 27. For this image, the inlet geometry has superimposed on top of the Schlieren to highlight the origins of the multitude of expansion waves present externally. It should be noted that some mass flow has entered the inlet, due to the 0.1mm gaps between the side plates and either side of the sliding door.

At approximately $t = 1.28$ seconds post trigger, the valve controlling the air flow (at a pressure of 3.5 bar) into the actuation piston is opened, resulting in the doors being retracted downstream. Fig. 28 shows the internal shock structure 0.02 seconds after opening the doors ($t = 1.3$ seconds). The expansion waves emanating from the tips of the retracting doors can be seen clearly at this unsteady stage. From here a Mach disc forms at the centreline of the inlet, as shown on Fig. 29 which is quickly swallowed by the inlet. It is also interesting to compare the profile of the external shocks at times $t = 1.3$ seconds and $t = 1.31$ seconds, where the shock angles have increased dramatically to a much blunter shock structure.

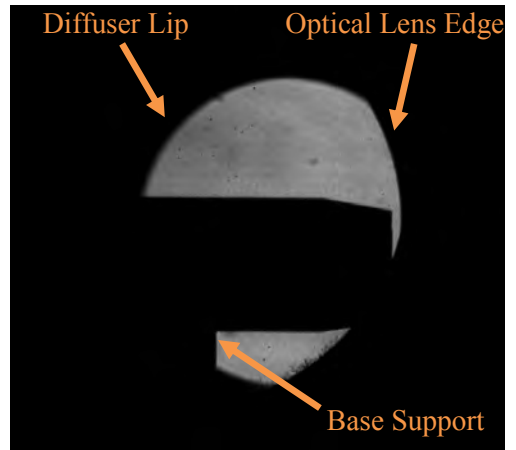


Figure 26: Prior to injection at $t = 0.88$ seconds

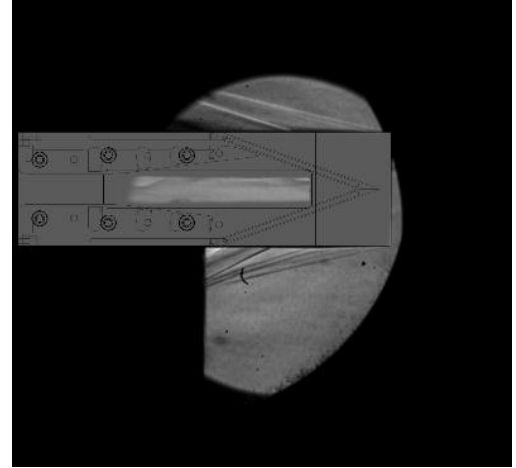


Figure 27: Steady solution prior to opening the doors at $t = 0.99$ seconds

Ultimately, a typical started supersonic regime is achieved at $t = 0.5$ seconds or 50 ms after opening the door, shown on Fig. 30. The inlet geometry has once again been overlayed on top of the Schlieren and it can be clearly seen that the internal shocks are emanating from the leading edge of the inlet geometry, with supersonic flow entering the combustor. It should be noted that the flowfield has not entirely reached a steady state as the shocks are not cleanly defined downstream of the reflection point. However due to the low frequency that the camera is operating at, the next image captured occurs just as the H3 wind tunnel blocks, caused by mass flow being diverged away from the diffuser lip by the door movement. That said, approximately 32 flow lengths have been undertaken prior to this tunnel blockage at the given test conditions and therefore it can be stated with confidence that steady started conditions have been achieved.

From this point onwards, the tunnel begins to block, due to the rising tunnel back pressure caused by insufficient capturing of the mass flow during the inlet starting procedure. Fig. 31 shows the flowfield just after imposing started flow, with the leading edge shocks moving upstream, with the shear layer of the flowfield beginning to close. Ultimately the tunnel was then shutdown, with the quantitative pressure and heat flux data showing a large spike in their respective values due back pressure rise ultimately leading to the flowfield traversing back upstream.

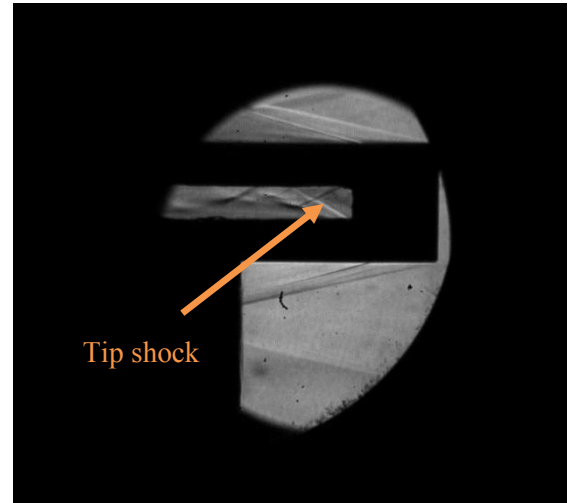


Figure 28: Flowfield at $t = 1.3$ seconds, showing tip shocks emanating from the sliding doors being retracted up over the scramjet body



Figure 29: Flowfield at $t = 1.31$ seconds, with a large increase in the external shock angles, with a Mach disc forming at the centreline of the inlet

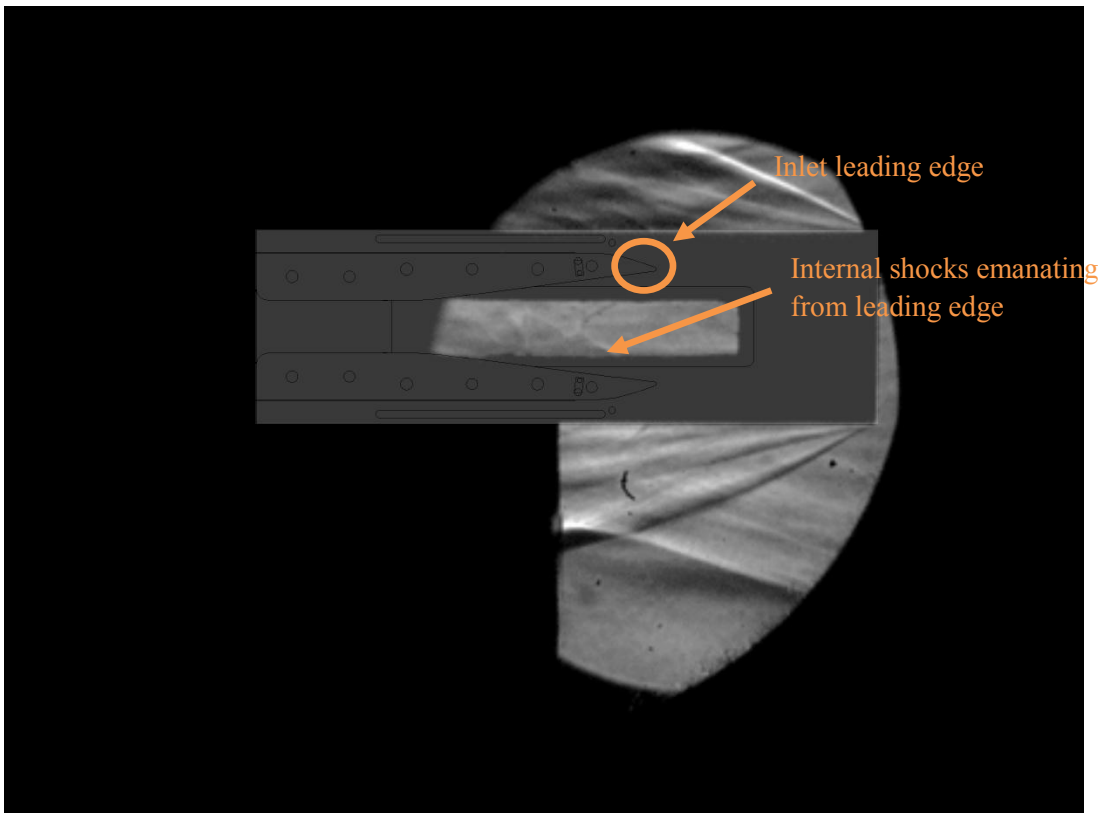


Figure 30: Started solution at $t = 1.33$ seconds, showing internal leading edge shocks

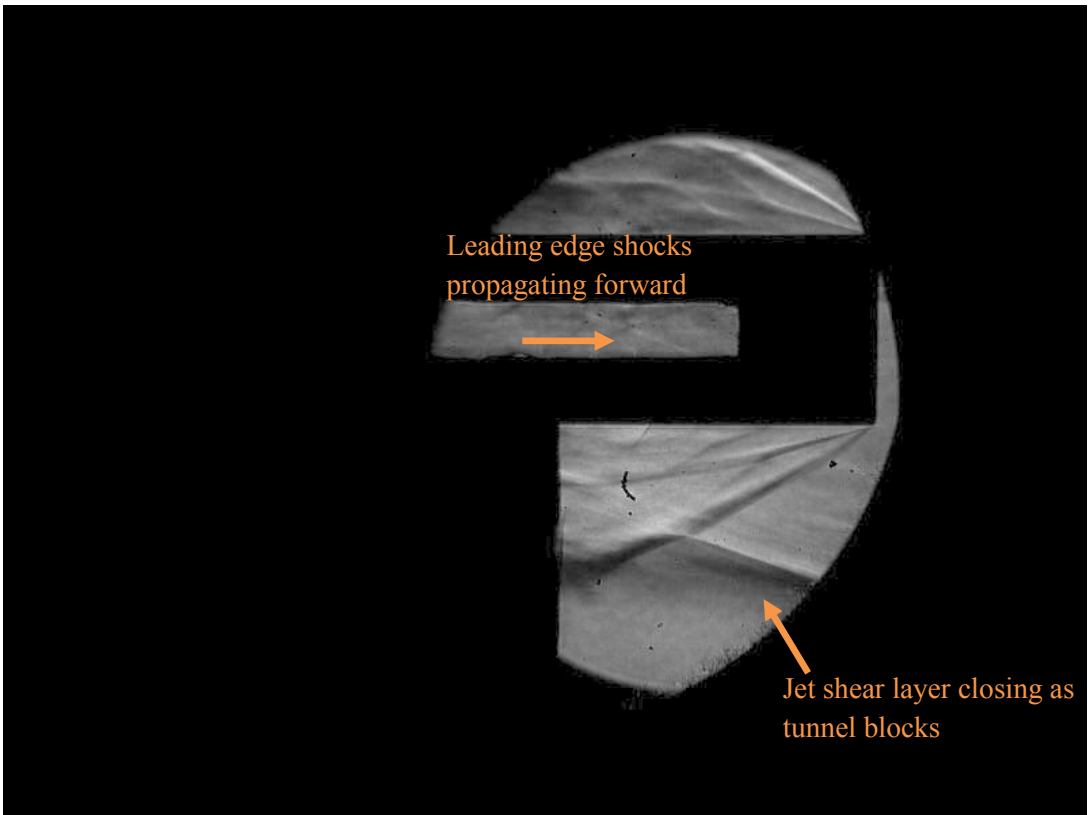


Figure 31: Schlieren at $t = 0.502$ seconds, showing the H3 tunnel beginning to block, with the shear layer change and internal shock forward propagation highlighted

5.2 Heat Flux Results

The unsteady heat flux results are outlined below. Fig. 32 shows the raw voltage output for sensor 2/1, sampled at 500 KHz.

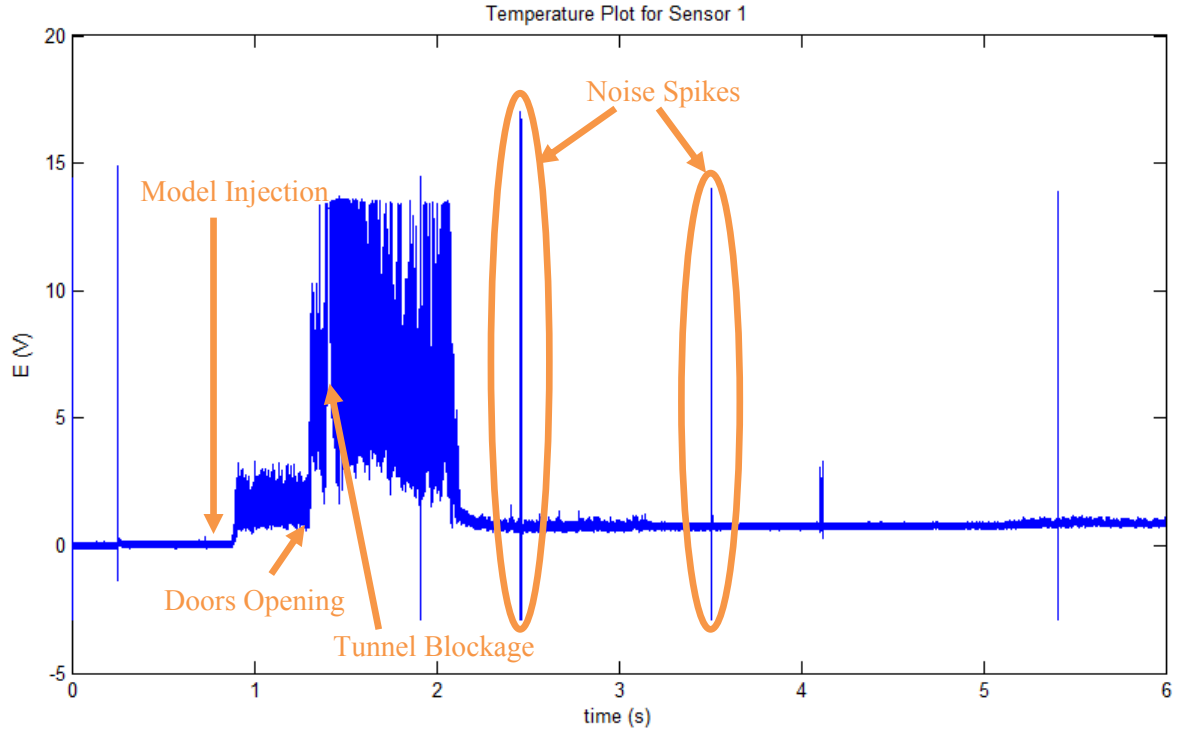


Figure 32: Raw Voltage Output from Thin Film Sensor 1, Array 1

It can be seen that the noise to signal ratio of the signal is extremely high, with large noise spikes at regular intervals during the test period. Several sensors, namely 1/1 and 2/5, unfortunately did not provide useful results as these resistance elements seem to be damaged after being installed into the model as a whole.

To eliminate the noise component of the signal, a 6th order Butterworth high pass filter has been applied to the raw signal. A comparison of the raw to filtered signal is shown on Fig. 33, with the red profile representing the filtered signal. In this case, the domain shows the area of interest prior to tunnel blockage. In particular key stages during the test period can be observed from the sensor signals. On Fig. 33, it can be seen that at approximately $t \approx 0.88$ seconds post trigger, a jump is seen in the signal. From the high speed camera Schlieren results, this point matches well with the time snapshot at which the model is being injected into the flowfield, as per Fig. 34. At this point it can be seen that some internal flow is present inside the inlet geometry prior to opening the doors, as illustrated on Fig. 34. The origins of this flow feature have been eluded to and will be discussed in following sections.

Additionally, a large spike in the signal is again seen at approximately $t \approx 1.302$ seconds post trigger, which correlates to approximately 0.02 seconds after the doors begin to retract. This flow state has been shown previously in Fig. 28, where the sudden rush of the flowfield into the inlet culminates in a large rise in signal amplitude due to the propagating shock structures impinging on the thin film array surface at the element locations. Indeed,

good correlation between the response of the thin film elements and the shock structures highlighted in the Schlieren results. Fig. 35 highlights one such occurrence where by extrapolation it can be seen that the shock impingement on the wall matches well with the heat transfer profile for sensor 1 at this time step ($t = 1.302$ seconds), as per Fig. 36. Therefore, it can be said that the profiles and peaks on the sensory output give a good description of the propagation of the shock structures.

From these results, it can be seen that certain flow phenomena captured by the Schlieren imaging can be verified by observing the signal output of the thin film arrays. At approximately 0.502 seconds after opening the doors ($t = 1.332$ seconds after injection), it has previously been seen that the tunnel begins to block. This is shown quantitatively in the filtered signal, where at the designated timestamp, a large rise is seen in the signal at this point as per Fig. 32, culminating with the signal regressing as the H3 tunnel is shut down.

A comparison of the heat flux profiles of the sensors along the centreline of the model is outlined on Figs. 37 and 38, gained by applying the calibration data outlined in Appendix A to the experimental output and then applying the previously mentioned Crank-Nicholson scheme to solve the 1D heat transfer equation (Eq. 1). A spike in heat transfer is noticed at the time of model injection, with the heat flux dissipating as the model surface reaches quasi-equilibrium. As the

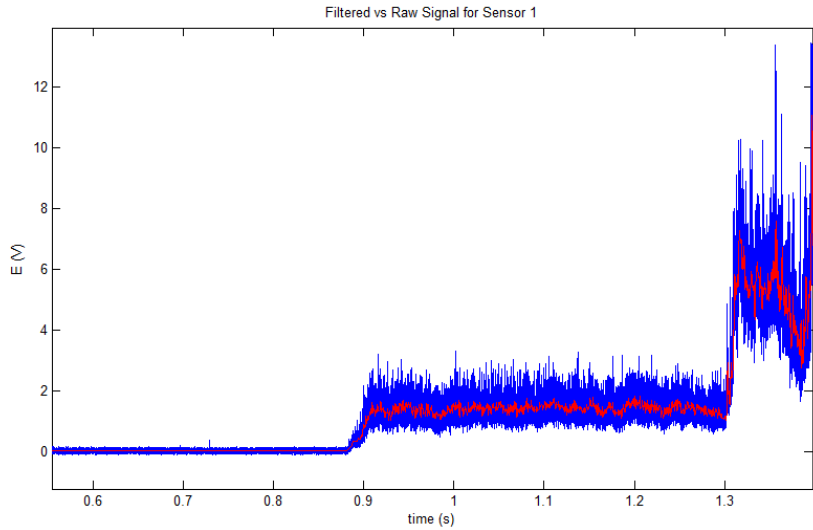


Figure 35: Raw vs. Filtered Signal for Sensor 1, with red profile denoting the filtered response

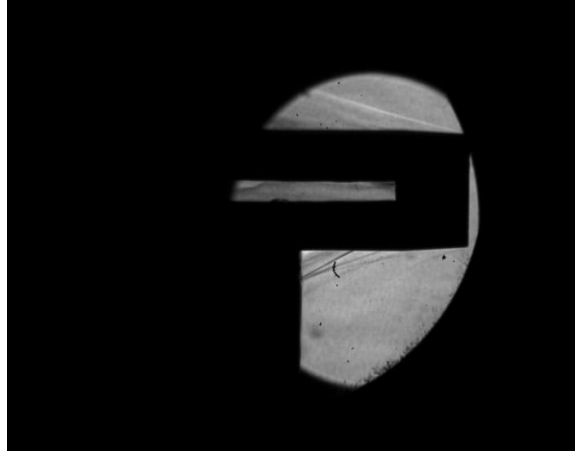


Figure 34: Schlieren snapshot showing internal flow during injection phase

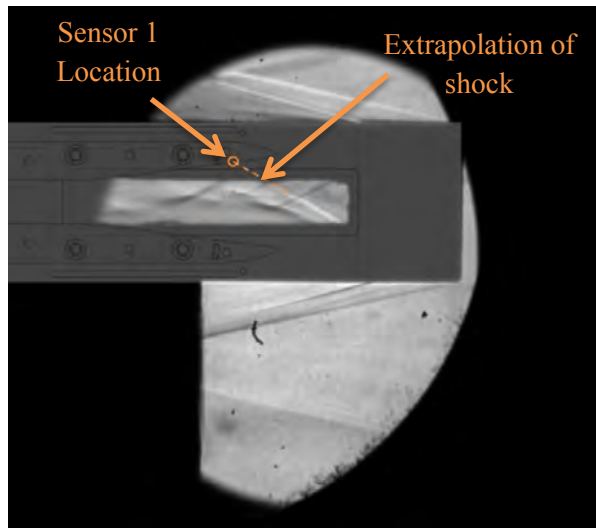


Figure 34: Shock impingement at sensor 1 location

doors are retracted at $t = 1.302$ post trigger, the heat flux again sees a sudden peak in response, with the response in this region indicated on Fig. 38.

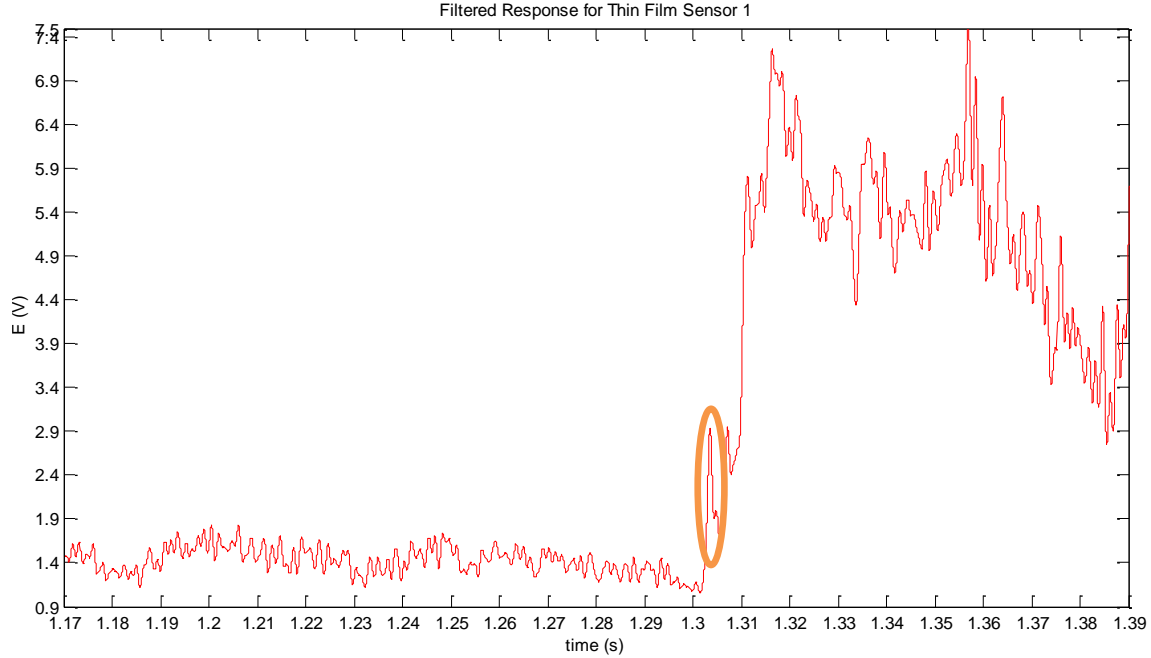


Figure 36: Filtered signal profile for sensor 2/1, highlighting a large spike in amplitude at approximately $t = 1.302$ seconds, correlating with shock impingement shown in Fig. 35 at the same time step

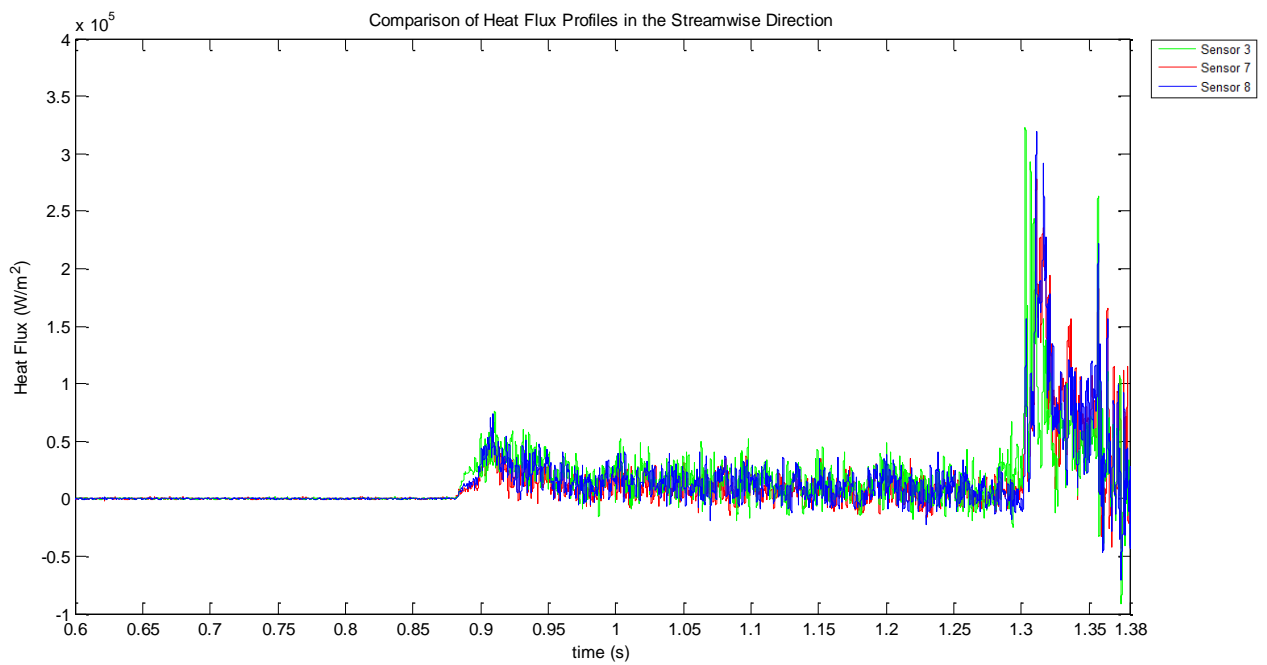


Figure 37: Heat Flux response at the wall for centreline sensors locations on thin film array 1 (bottom half of model)

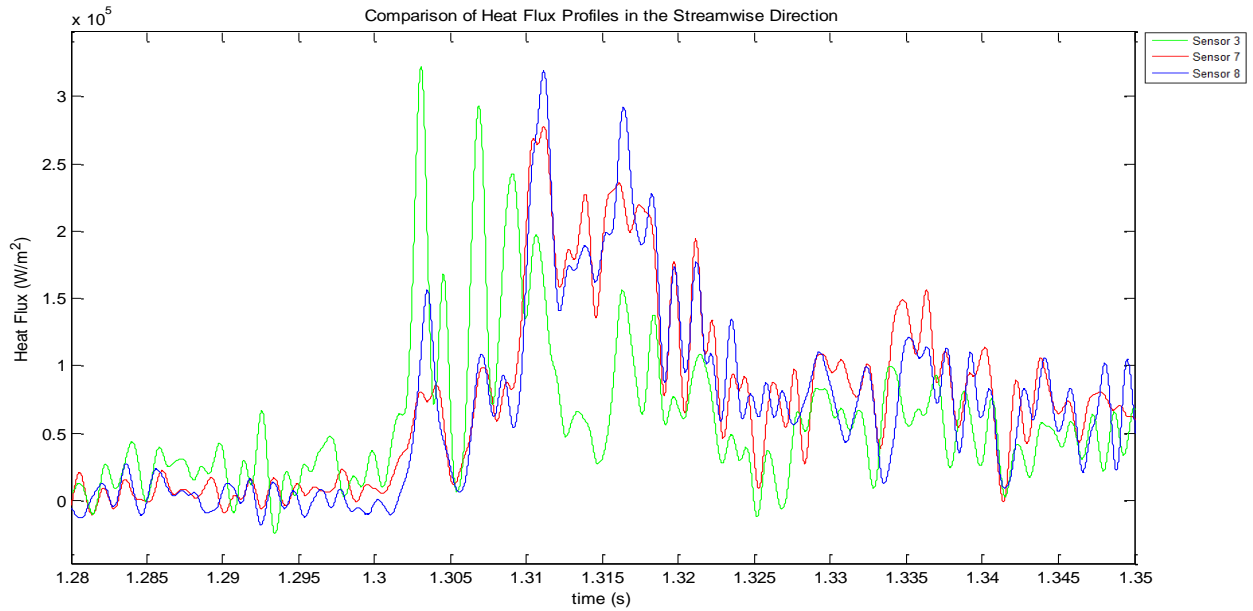


Figure 38: Heat Flux Comparison of Block 1, with the window displaying the domain at which the doors are retracted ($t = 1.3$ seconds) until quasi-steady started inlet conditions are obtained

Fig. 38 can be used to determine progression of the flowfield during the inlet starting procedure. During the initial stages of the inlet starting procedure, the large influx of mass flow into the internal geometry results in a large rise in heat flux. As expected, the amplitude of this initial rise is significantly higher for the more upstream sensor 1/3 than the downstream sensor elements 1/7 and 1/8. It is also interesting to note that the peaks in heat flux signal for the centreline sensors, over the course of the entire inlet starting procedure, appear to be in phase with one another. Figs. 39 and 40 display the heat transfer profiles for sensors 2/2 to 2/6 on the upper half of the model geometry, which are spread in a line laterally approximately 17.3 mm downstream of the tip of the array, as per Fig. 20. This comparison can be used to gain an understanding of the 3D effects present in the inlet due to the side plates that house the inlet geometry.

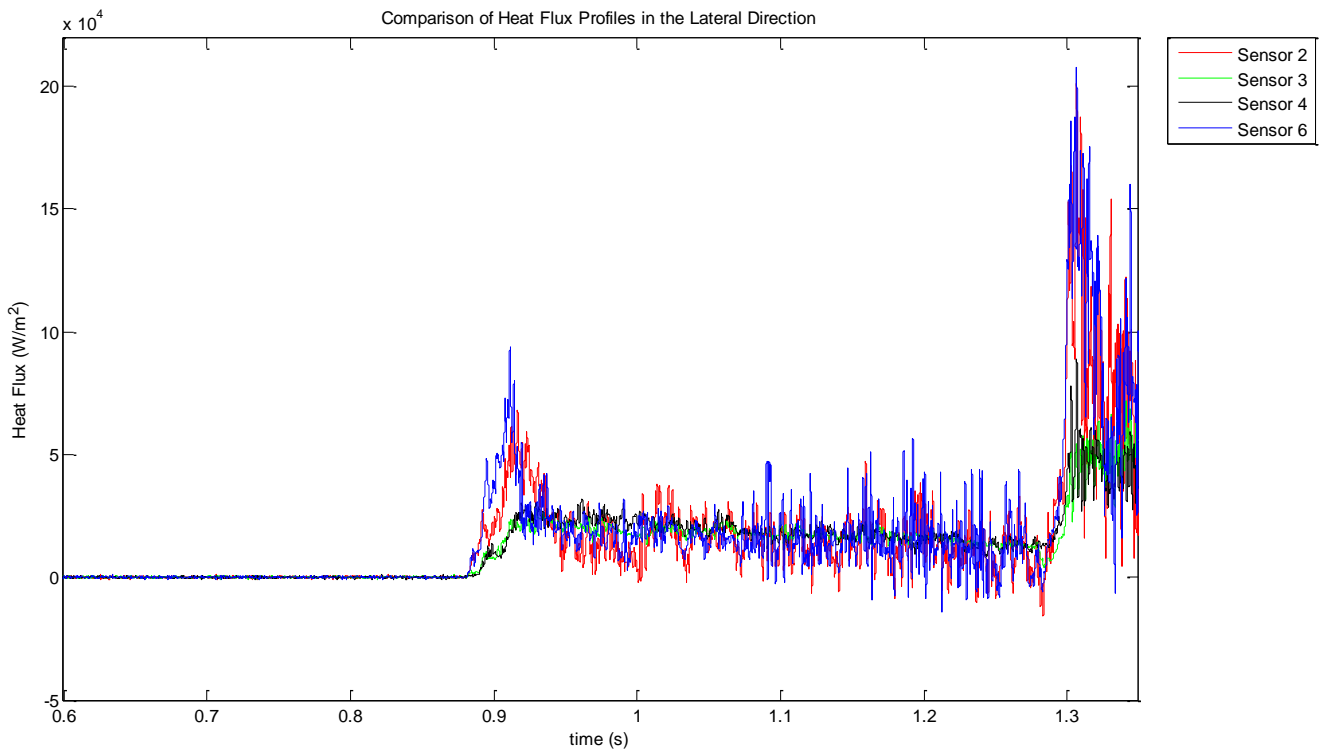


Figure 39: Heat Flux Profiles of Laterally Spaced Thin Film Elements, showing variance due to 3D effects

At the point of injection, it can be seen that the most outer sensory elements (2/2 and 2/6) experience a more severe increase in heat flux. In this case the doors are closed and therefore this rise is due purely to mass flow passing through the slots on either side of the door. The more centrally located elements 2/3 and 2/4 do not see as sharp an increase. Fig. 40 displays the time domain at which the sliding door retraction procedure is undertaken. The outer sensors once again provide heat flux profiles much higher than the more centrally located sensors 2/3 and 2/4. Indeed the difference in heat flux response when comparing the external to internal thin film elements is significant, with potential causes other than the side plates discussed in following sections. Fig. 40 also highlights that the peaks in heat flux occur at similar time steps, particularly at the end of the inlet starting procedure where steady conditions are being approached in the combustor. Note however that while comparisons have been made between the outermost (sensors 2/2 and 2/6) and the innermost (sensor 2/3 and 2/4) element heat flux profiles, these sensors lie at varying distances from the centreline (e.g. sensor 2/2 and 2/6 located 5.65 and 7.2 mm from the model centre respectively) and as such Fig. 40 has not been used to compare lateral symmetry about the centre plane.

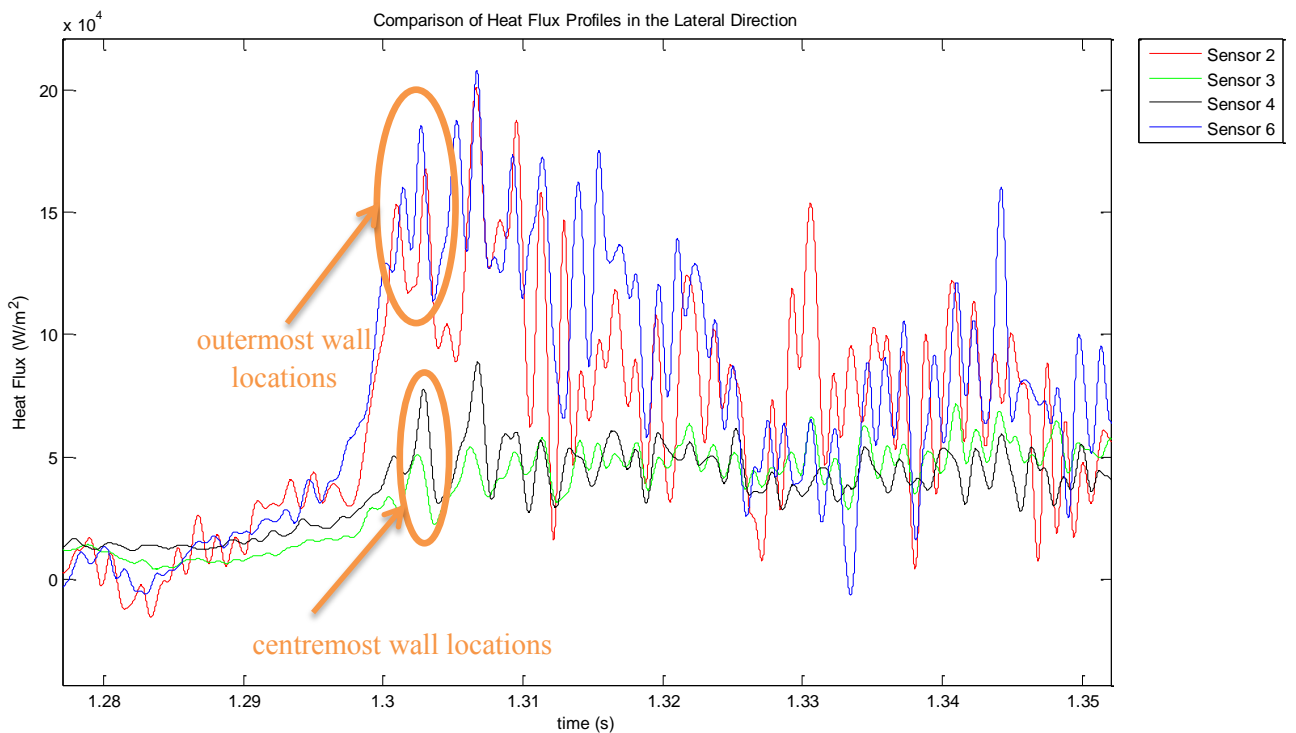


Figure 40: Lateral heat flux comparison, 17.3mm downstream of array tip. Regions of variance for the external sensors have been circled

It is important to also compare the heat flux profiles of elements on the top and bottom halves of the model geometry, at the same x and lateral locations, primarily to investigate whether both doors have opened simultaneously, or whether variance in tension has resulted in differences in door opening times relative to one another. To achieve this, heat flux profiles of element 3 on both halves of the inlet geometry have been displayed below on Fig. 41.

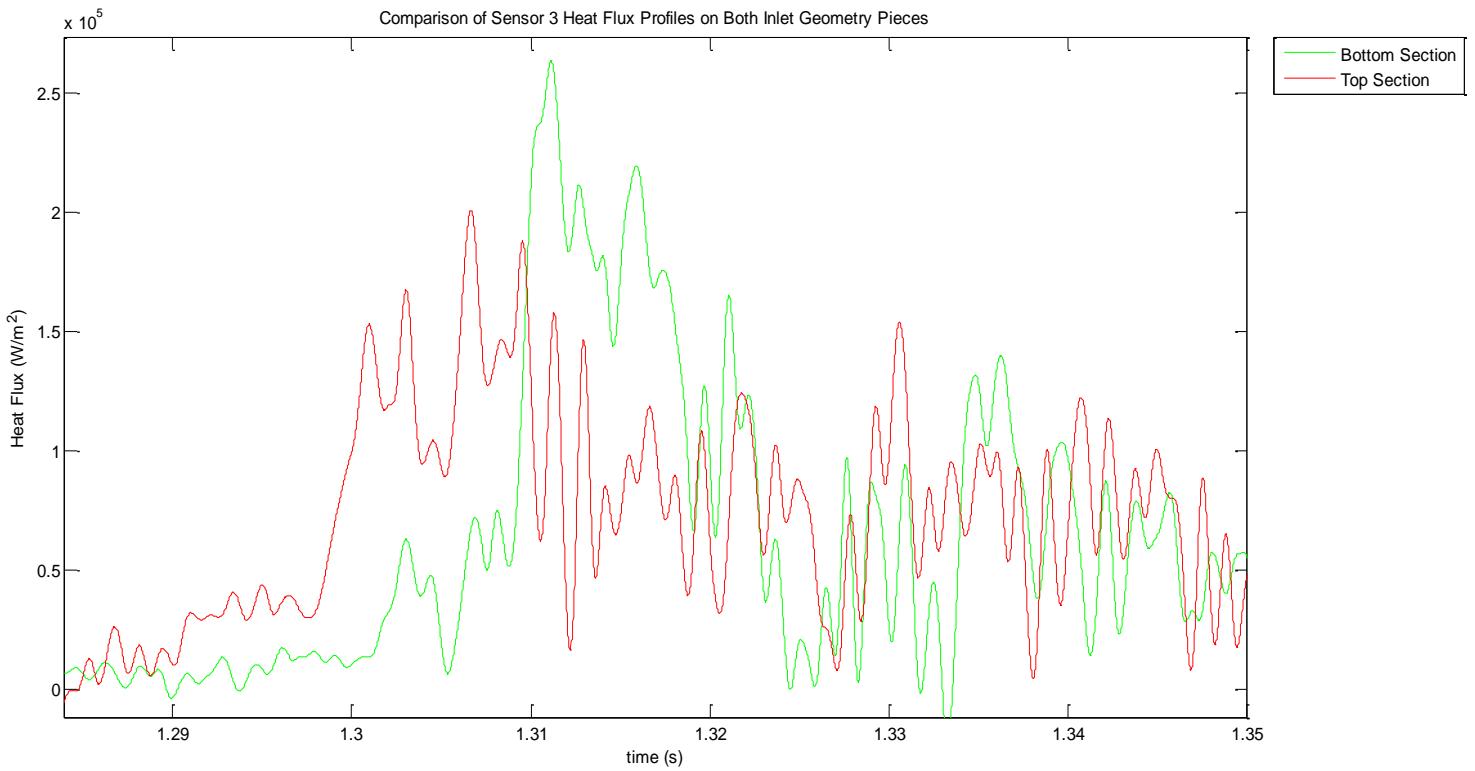


Figure 41: Comparison of Element 2 Profiles, for both thin film arrays on each geometry section, highlighting the time domain of

It can be seen that there is a significant difference in the profiles of the two sensors, with the top wall sensor location experiencing a much higher heat flux. This suggests that the top door may have in fact opened slightly prior to the bottom door. By re-examining the Schlieren results at the beginning of the inlet starting procedure, it can be seen that the strong shocks emanating from the leading edges of the sliding doors on Fig. 28 extend into the inlet at varying angles as per Fig. 42. As the reflection point is higher than the centreline and by recalling that the initial motion of the door is dominated by its rotational component, it can be stated that the top door at this stage has been retracted further up over the body of the inlet than the bottom door, as due to the rotational effects of the door movement, a stronger shock at a more normal angle



Figure 42: Schlieren snapshot at $t = 1.302$ seconds, with the difference in door edge shocks displayed by highlighting that the reflection point of the shocks does not lie on the centreline, but above

will result as the door is further retracted, which would explain the difference in shock angles and thereby explain the difference in heat flux profiles on either side of the inlet. Therefore it can be said that while the change in displacement of the two doors is coupled as per previous discussion, it appears that the initial tension in the upper door is higher than its lower counterpart, resulting in the sliding door retraction mismatch.

With this in mind a Stanton number distribution on both halves of the model geometry was taken at $t = 1.34$ seconds, which from the Schlieren results represents the period at which started flow conditions have been achieved. In this case, the Stanton number has been calculated via the modified method developed by Tirtey⁹, whereby the total temperature is used in the calculation rather than the adiabatic wall temperature and is defined per Equation 4:

$$St_{mod} = \frac{\dot{q}}{\rho_\infty u_\infty c_p (T_o - T_w)}$$

Equation 4: Modified Stanton Number⁹

Additionally a preliminary 2D numerical simulation of the experimental configuration was undertaken, with the Stanton number distribution extracted from the end started flow solution. While not a true representation of the experimental results, the numerical profile gives a good description of the expected profile of the experimental distributions, as well as a means of checking whether the experimental magnitudes are of the right order. The Stanton number distributions along both arrays are outlined below on Fig. 43, with sources or error and uncertainty included via error bars:

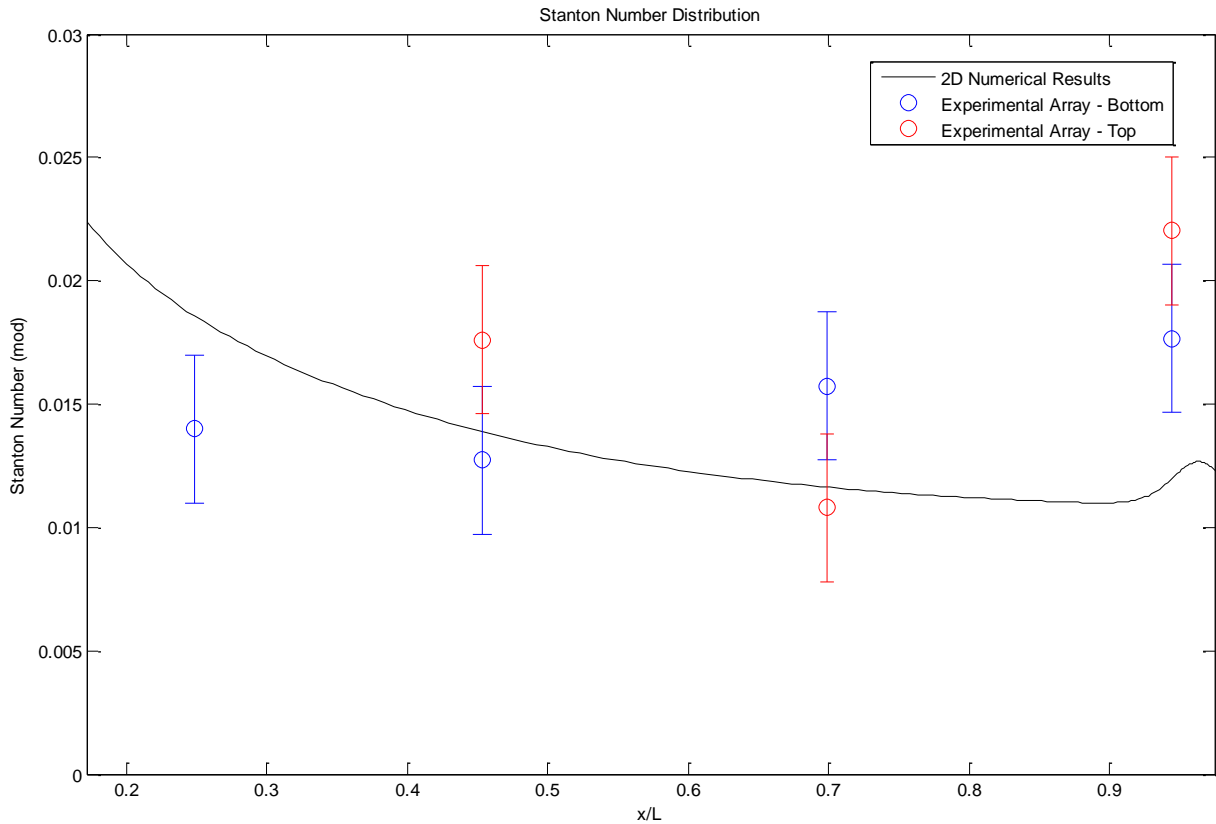


Figure 43: Stanton Number distribution, showing experimental results compared to preliminary 2D CFD

From the above distributions it can be seen that the experimental results are relatively close to those expected by the 2D simulation. However it can be seen that the numerical solution over estimates near the leading edge ($x/L < 0.3$) and underestimates near the combustor. The reason for this most likely lies with the way in which the inlet wall boundary condition is imposed for the numerical solution. When computing this simulation, an isothermal wall boundary condition was imposed ($T \approx 340$ K), taken from the average measured experimental wall temperature at the started flow conditions. As a result of this uniform approach to describing the wall boundary condition, the numerical capturing of the viscous region near the wall may not be properly represented and hence, the heat flux and temperature components of the Stanton number calculation may be not entirely accurate. That said the experimental conditions do provide a relatively good comparison to the numerical profile, particularly when considering that the 3D effects outlined previously have not been included.

5.2 Pressure Results

Fig. 44 as outlines the raw and filtered signal output for pressure sensor 1/4, where it can be seen that the profile over time strongly resembles that which is observed previously via the thin film heat flux results. This is better observed on Fig. 45 where the time period at which the sliding doors are opened is highlighted.

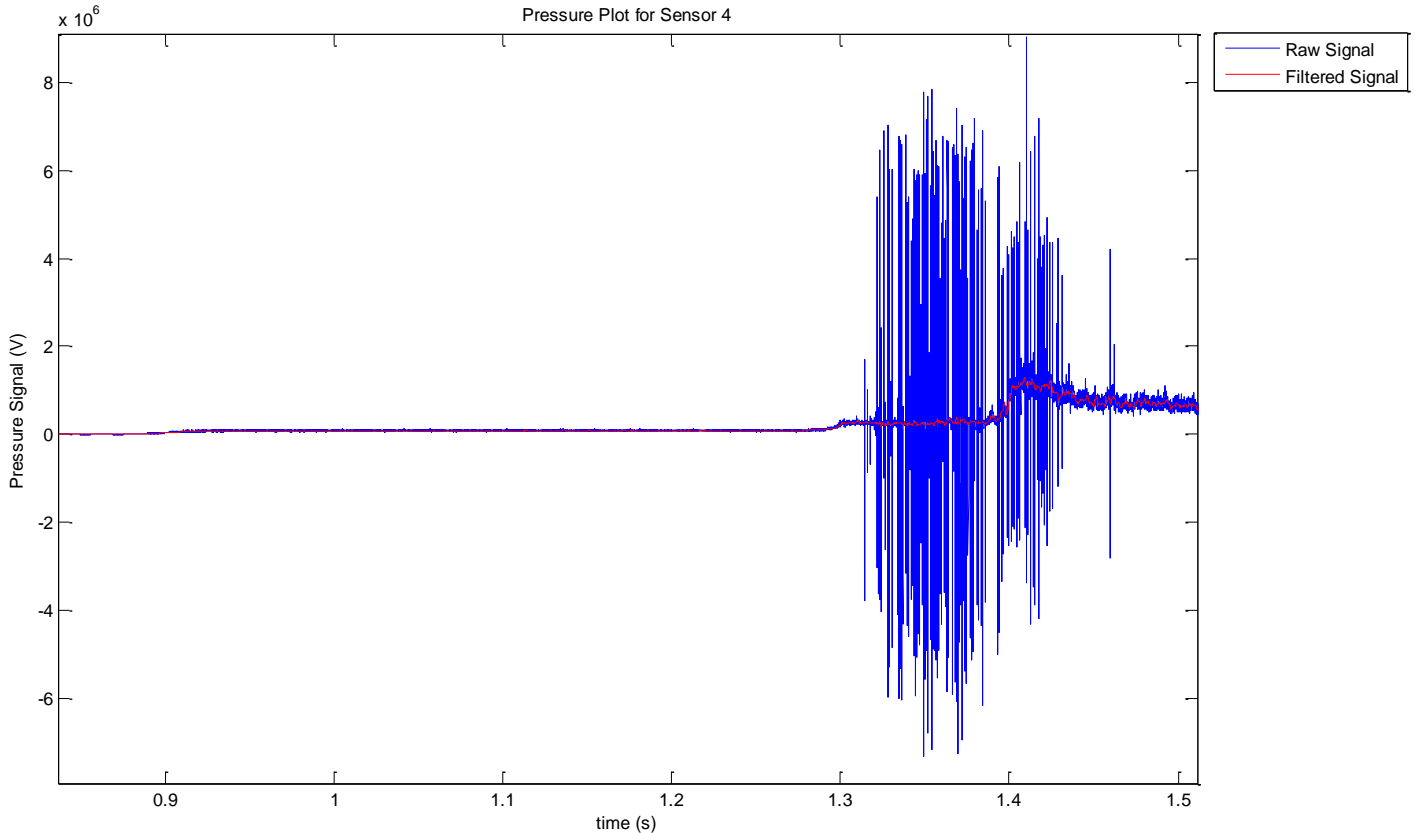


Figure 44: Filtered vs. Raw Signal Comparison for Pressure Sensor 4

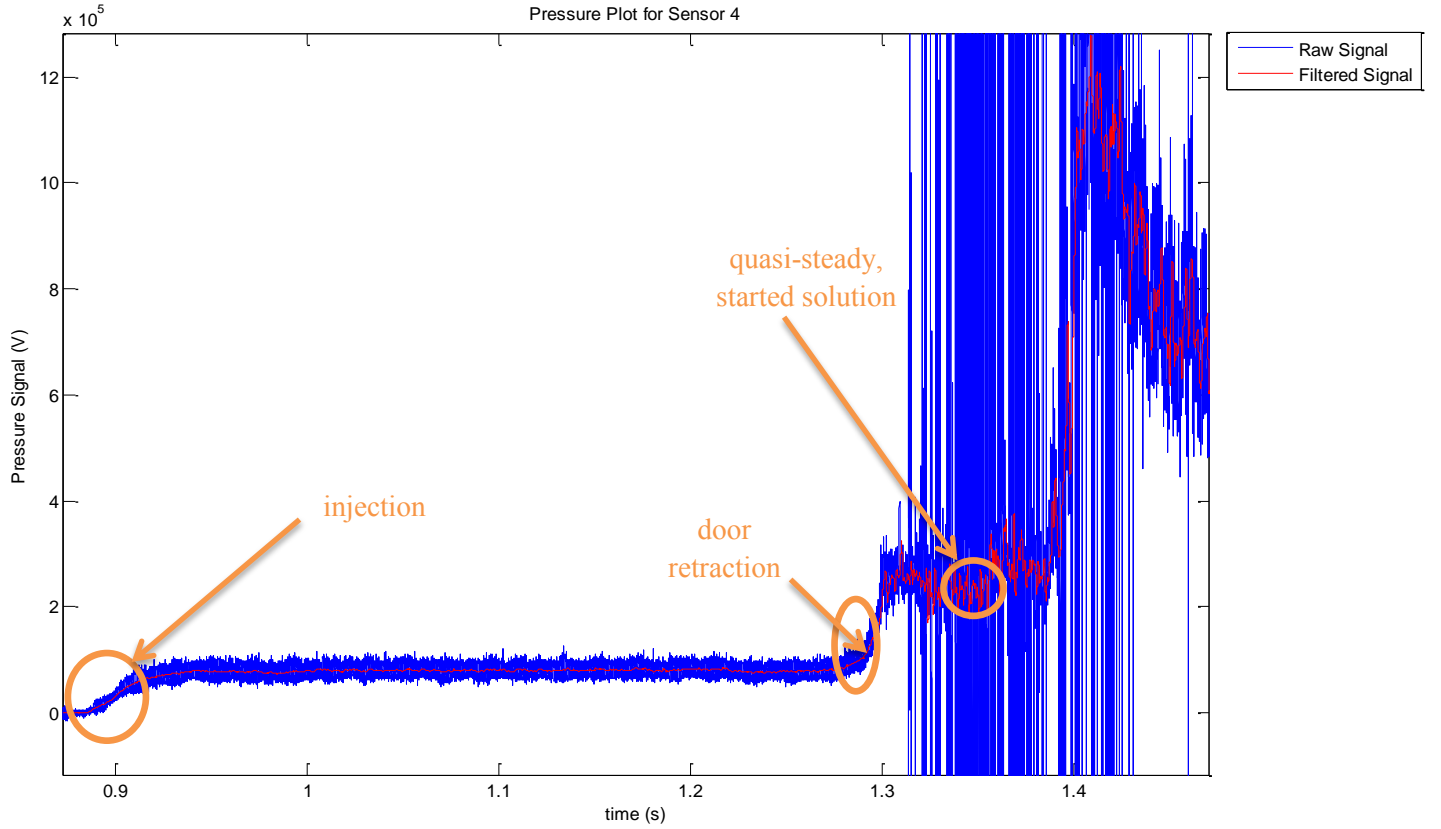


Figure 45: Pressure sensor 4 signal, with key attributes highlighted

The rise due to model injection can once again be seen, with the response due to the retraction of the doors ($t \approx 1.28$ seconds) being clearly visible. The calibration curves, outlined in Appendix A, were then applied to the filtered pressure signals to obtain the pressure profiles of the 8 sensors during the test time, with the result plotted on Fig. 46. It should be noted that during installation it appears that sensors 1/1 and 1/3 on the bottom half of the model geometry have been damaged, with no measureable output obtained.

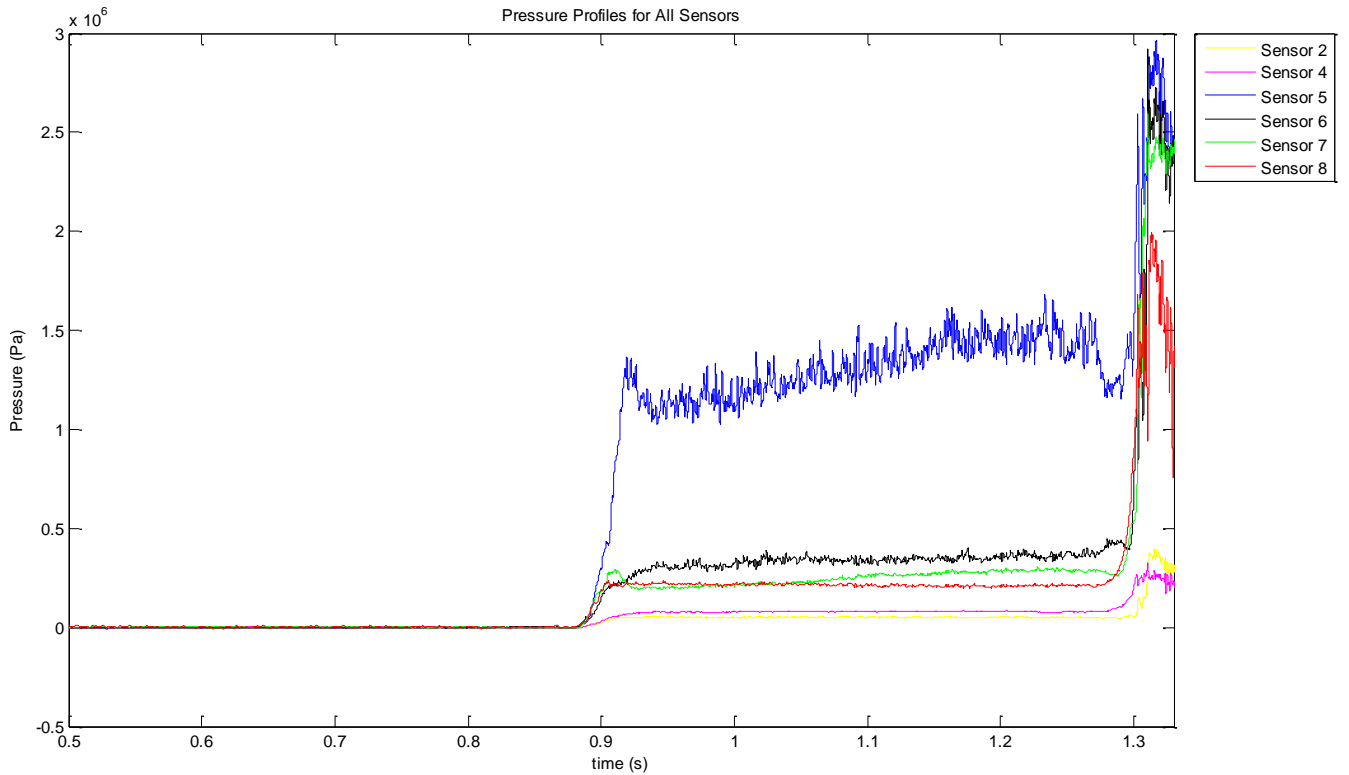


Figure 46: Pressure profiles for all sensors, truncated at the point at which
Distribution A: ^{started flow conditions are achieved} Approved for public release; distribution is unlimited.

From Fig. 46 several key observations can be made. Firstly, it can be seen that pressure sensor traces on the lower inlet geometry section (sensors 2 and 4) are significantly lower than those observed on the upper model section (sensors 5 through to 8), in some cases up to an order of magnitude. This is concerning as it implies that the jet provided by the tunnel is not aligned at 0 degrees AoA. However, it can also be seen that the maximum measure pressure by sensor 5 approaches a value of 3 MPa or 30 bar pressure, which is not feasible as this is larger than the freestream stagnation pressure for this test run. As such, it is therefore evident that the calibration profiles outlined in Appendix A does not properly represent the response of the Entran transducers. However, techniques can be used such that the pressure data can be used to compare future studies.

6.0 Discussion and Sources of Error

When employing the sliding door inlet starting mechanism, started flow conditions were achieved for a high contraction ratio scramjet inlet geometry at Mach 6 in the H3 Wind Tunnel Facility. As per the results highlighted in previous sections, these started flow conditions were maintained for a total of approximately 32 flow lengths for the inlet reference length used (0.06m). This magnitude is of a high enough quantity to suggest that steady conditions were achieved. Unfortunately due to the limitations of the H3 diffuser size, it has been shown that blocking of the tunnel then soon followed after acquiring this started solution. This is shown visually below on Fig. 47, where the raw signal output of the H3 vacuum pressure transducer has been outlined:

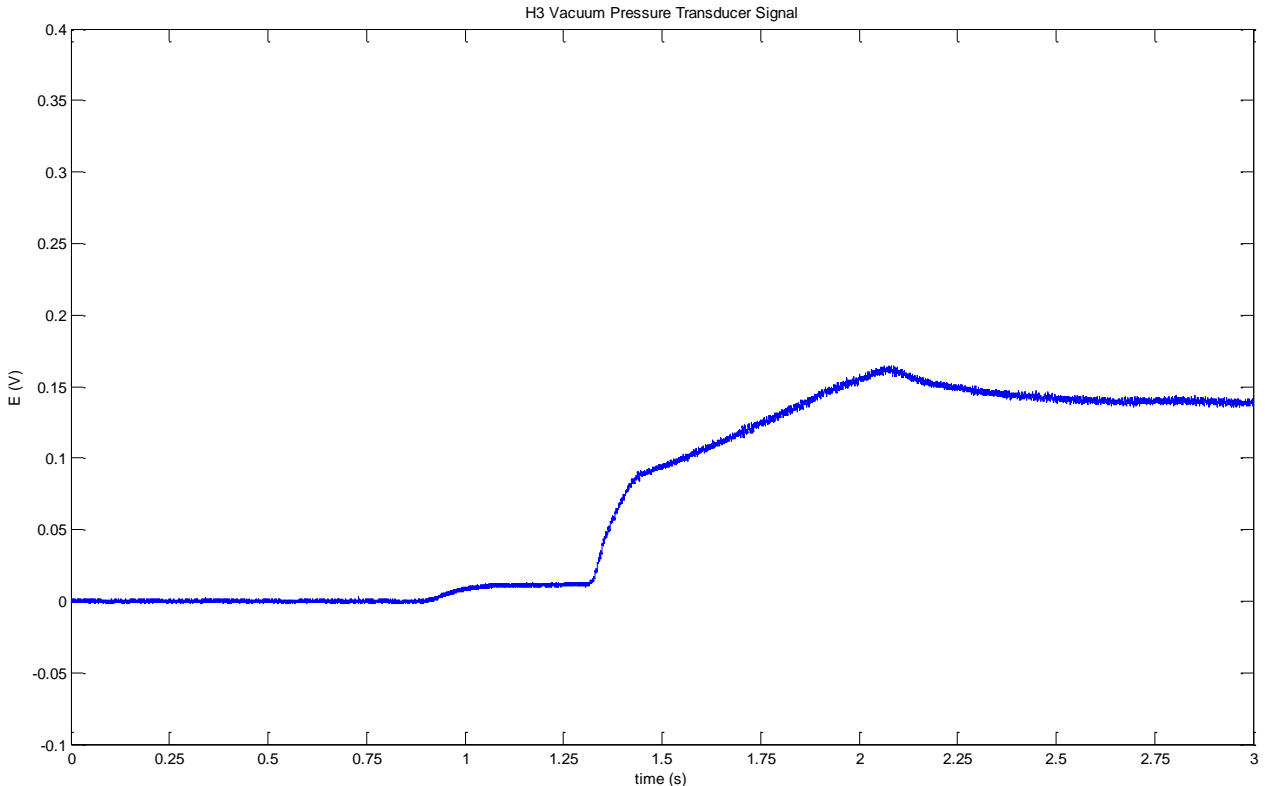


Figure 47: H3 Vacuum pressure profile, showing rises due to model manipulation

As can be seen the tunnel back pressure rises as a result of model injection at $t = 0.88$ seconds, with a significant jump then observed as the doors are retracted at $t = 1.28$ seconds. Physically what is happening at this stage is that the changing inclination of the sliding door is resulting in a significant portion of the jet mass flow being diverted around the diffuser. This is in of itself not a serious concern with regards to the test period between 1.28 and 1.33 seconds. However, as a result of this blockage, the model then proceeds to experience extremely high temperatures as a result. This culminates in the Senflex thin film arrays experiencing temperatures in excess of 120 degrees Celsius, which ultimately resulted in the adhesive used to secure the thin film array beginning to melt. As such this lead to the end of the test campaign, which has ramifications with regards to the repeatability of the test results. As such, further tests are currently being completed on site at the Von Karman Institute.

A large amount of noise was visible in the raw output from the instrumentation, particularly in the thin film element signals. Indeed, fluctuations were noticed for all channels prior to operating the tunnel, suggesting that noise generated from the nearby plasmatron, which was operating at the same

time as this test campaign, was “picked up” by the H3 wind tunnel instrumentation. Additionally the noise to signal ratio is significantly higher for one of the heat transfer boxes when compared to the other, as per Fig. 48. It is most likely that this is due to the fact that one of the three internal circuitry boards from “Heat Box 1” was damaged previously. These boards are placed in series and as such this damaged board was simply removed from the circuit prior to testing and calibration. That said it is possible that this issue may have caused the increased noise present in the output. However while this is not ideal, the integrity of the results gained seems to be assured, as the thin film results have been shown to accurately track the phenomena captured via the Schlieren imaging.

Indeed the Mach disc observed on Fig. 29 is one such phenomenon that is of high interest. As part of previous numerical inlet starting studies^{1,2,3} it was seen that the continued propagation of this Mach disc into the combustor was one of the major contributing factors that determined whether a started solution was ultimately obtained. It is important to note that this phenomenon was present for a wide variety of varying inlet starting mechanisms, which manipulated the inlet design at different locations along the length of the inlet. While it could be that this structure is a relic of the inherent similarities of scramjet inlet geometries, this phenomena is one such feature that will be investigated in more detail.

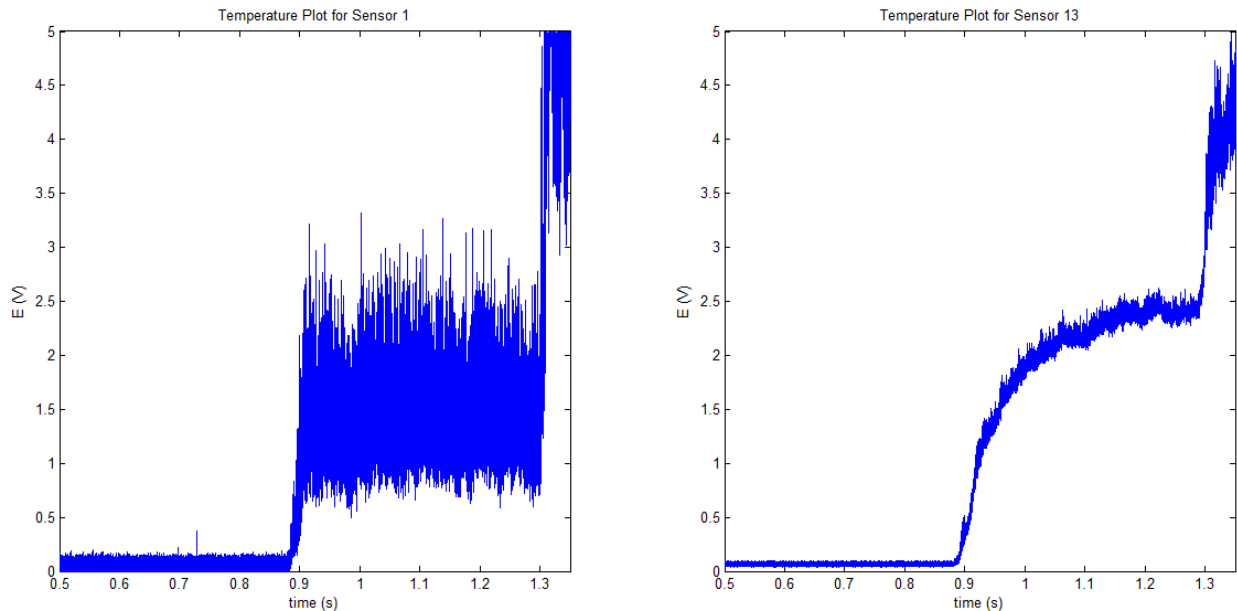


Figure 48: Comparison of Signals gained from each Heat Transfer Box

Also, it is interesting to note that during the inlet starting procedure, vague streamline-like flow structures are evident on the Schlieren output downstream of the propagating Mach disc, as per Fig 49. These lines are in fact evidence of transition on the side walls of the inlet. In this case the roughness element could potentially be a result of the flush mounted window being slightly out of plane with the rest of the interior.

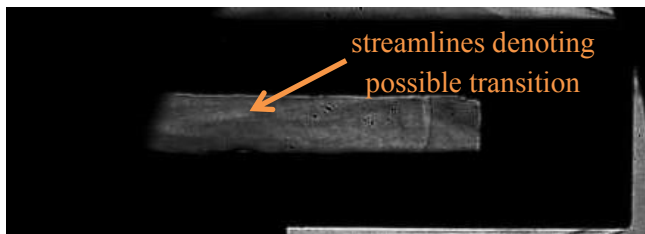


Figure 49: Evidence of presumed transition on the side plate inner walls

Finally, as per the previous section highlighting the pressure transducer data gained from the experimental campaign, it is difficult at this time to determine whether these results show any meaningful data, as it appears that the calibration data may no longer accurately describe the relationship between voltage and pressure. However by scaling the pressure data with regards to its highest measured peak, the trends noticed in the pressure profiles can be used as means of verifying whether the planned numerical simulations of the experimental setup accurately capture the evolution of pressure during the inlet starting procedure.

With regards to the model design, several changes can and should be made to the model configuration as further tests are undertaken. In particular, the presence of the 0.1mm gaps between the sliding door and the side plate is one feature which is an unintended product of the inlet starting process. These gaps are present as it was intended that the motion of the doors be captured during the inlet starting process as much as possible. As metallic materials would need to be used in order to compensate for the pressures that the sliding doors would experience prior to opening, it was feared that the doors would scratch the flush mounted quartz window in the event that the door was not aligned perfectly with the flow. As such it was initially intended that a Teflon piece be added on either side of the sliding door such that in the event of contact the window would not be damaged. However due to manufacturing limitations this was not plausible. Ultimately the design team decided that the gap would be left in place, with the measured properties prior to opening the door forming the basis for the initial conditions used in the planned numerical representation of this experiment.

The other major limitation with this experimental model configuration is in regards to tracking the motion of the sliding doors. Currently the main method of tracking the door is via extrapolating the leading edge shocks back the location of the sliding door leading edge. As the pathing of the door motion is fixed via the profile of the carved grooves, the degree of door retraction can be calculated. Ideally however in future tests it would be greatly beneficial to track the door via an electronic means, such as a small resistance element, particularly as it was seen that the doors were not entirely in sync while being retracted. With respect to the overall model, the installed optical window appears to be smaller than that which would be ideal. A window of larger size however was not installed was purely because of the model scaling requirements of the H3 tunnel with regards to blockage. This in collaboration with the minimum dimensions of the fasteners and pins required to secure the model together, resulted in an upper limit on the size available for the window to be mounted. Additionally a longer window in the stream wise direction was impractical as the area available for light to pass through was also limited by the outer tunnel window edges and the location of the tunnel diffuser.

The most important result of this window limitation is that the boundary layer was not able to be accurately captured visually during the inlet starting process. This is regrettable as the observing the viscous region during the inlet starting procedure would have provided an excellent means of investigating phenomena such as Shockwave Boundary Layer Interaction (SWBLI). With that said the quantitative data obtained from the Senflex arrays will provide a means of validating the accuracy of numerical simulations when capturing this region.

7.0 Future Activities

As outlined in the overall objectives of this report, the experimental campaign undertaken at the Von Karman Institute of Fluid Dynamics is but one part of a larger ongoing inlet starting study. As part of this study, the next phase involves a complete numerical recreation of the experimental campaign by way of the commercial code CFD++¹⁰ and consists of several key stages:

- An initial 2D RANS time accurate simulation investigating whether the inlet starting procedure matches the event scale observed via the Schlieren results
- A further 3D time-accurate study simulating all components present in the experimental configuration

The 3D results will then be compared to those gained via the experimental campaign, with a report due in July 2012. In particular, it is hoped that the numerical simulations will provide further insight into the flow physics, particularly the effects of viscosity and separation, and to fill in the gaps left by the lower than ideal high speed camera frequency. It is additionally planned that further numerical parametric studies will be completed, aimed at investigating the influence of:

- speed at which the doors are retracted (i.e. simulating variance in the air supply pressure to the pneumatic piston)
- simulating varying freestream conditions to gauge the applicability of the sliding door mechanism over a range of possible situations

It is hoped that these numerical simulations will firstly provide an accurate recreation of the experimental campaign, as well as a more clear understanding of the physical flow phenomena present during the sliding door inlet starting procedure. Ideally these results will go some way to providing a more clear understanding of inlet starting processes in general, as currently little is known of the intermediary steps along the path to achieving either solution for an inlet located in the dual solution region.

Additional experimental tests are also currently being conducted at the Von Karman Institute, with the aim being to show repeatability with regards to the results shown in this report.

8.0 Conclusions

This report has outlined the premise and results of the inlet starting experimental campaign undertaken at the Von Karman Institute, Belgium, aimed at investigating the sliding doors inlet starting mechanism for a hypersonic scramjet inlet. This campaign provided the first step upon a much larger inlet starting investigation, with the obtained results providing a backbone for comparison to future 2D and 3D transient RANS numerical studies.

The test campaign was undertaken in the H3 Wind Tunnel Facility, which provided a jet at Mach 6 at various reservoir pressures, with variance in Reynolds number used to simulate changing altitude conditions. Successful inlet starting was achieved for a 2D scaled representation of the SCRAMSPACE-I geometry, simulating an altitude of approximately 29 km. Schlieren visualisation techniques showed that supersonic conditions were indeed obtained in the inlet for approximately 32 flow lengths. Senflex thin film arrays, located on the inner surfaces of the inlet, captured the transient heat flux progression at different locations along the inlet. These profiles accurately captured the phenomena observed via the Schlieren imaging, in particular the propagation of shock structures into the inlet during the inlet starting procedure. Stanton number distributions along both arrays were extracted and showed a close comparison to those expected from numerical simulations reconstructed test flow conditions, which lends credibility to the integrity of the heat flux results. Additional pressure measurements were taken, with 8 Entran EPIH-11 sensors mounted flush with the inlet internal. However due to apparent calibration errors the true measured pressure magnitude in terms of Pascals was not captured. That said the data can indeed be used to compare to future numerical simulations via amplitude scaling.

9.0 Bibliography

¹Timofeev, E.V., Tahir, R.B. and Mölder, S., “On recent developments related to flow starting in hypersonic air intakes”, AIAA-2008-2512, 15th AIAA International Space Planes and Hypersonic Systems and Technologies Conference, Dayton, OH, Apr 2008.

²Veillard, X., Tahir, R.B., Timofeev, E.V. and Mölder, S., “Limiting Contractions for Starting Simple Ramp-Type Scramjet Intakes with Overboard Spillage”, Journal of Propulsion and Power, accepted, DOI: 10.2514/1.34547, 2008.

³Ogawa, H., Grainger, A. and Boyce, R.R. “Inlet starting of high-contraction axisymmetric scramjets”, In: Van Wie, Proceedings of 16th AIAA/DLR/DGLR International Space Planes and Hypersonic Systems and Technologies Conference. *16th AIAA/DLR/DGLR International Space Planes and Hypersonic Systems and Technologies*, Bremen, Germany, (7401-1-7401-17). 19-22 October, 2009.

⁴Ogawa, Hideaki, Grainger, Alexander L. and Boyce, Russell R. “Inlet starting of high-contraction axisymmetric scramjets”, *Journal of Propulsion and Power*, 26 6: 1247-1258, 2010.

⁵Schreivogel, P., Paniagua, G. Flat Plate Transition Study – H3 Wind Tunnel Facility. Project Report 2008-26, Von Karman Institute, November 2009.

⁶Iliopoulou, V., 2005, „High Frequency Gas Temperature and Surface Heat Flux Measurements“, PhD thesis, Von Karman Institute, Belgium.

⁷Miller C.G., 1981, „Comparison of thin-film resistance heat transfer gauges with thin skin transient calorimeter gages in conventional hypersonic wind tunnels“, NASA Technical Memorandum 83197

⁸Anderson J.D., 1990, „Modern compressible flow with historical perspective“, McGraw-Hill series in aeronautical and aerospace engineering, McGraw-Hill, Inc, ISBN 0-07-001673-9, United States of America

⁹Tirtey, S.C. “Characterisation of a Transitional Hypersonic Boundary Layer in Wind Tunnel and Flight Conditions”, PhD thesis, Universite Libre de Bruxelles, Von Karman Institute, 2008.

¹⁰CFD++, Software Package, Ver. 8.11, Metacomp Technologies, Inc., CA, 2009.

Appendix A – Calibration Curves

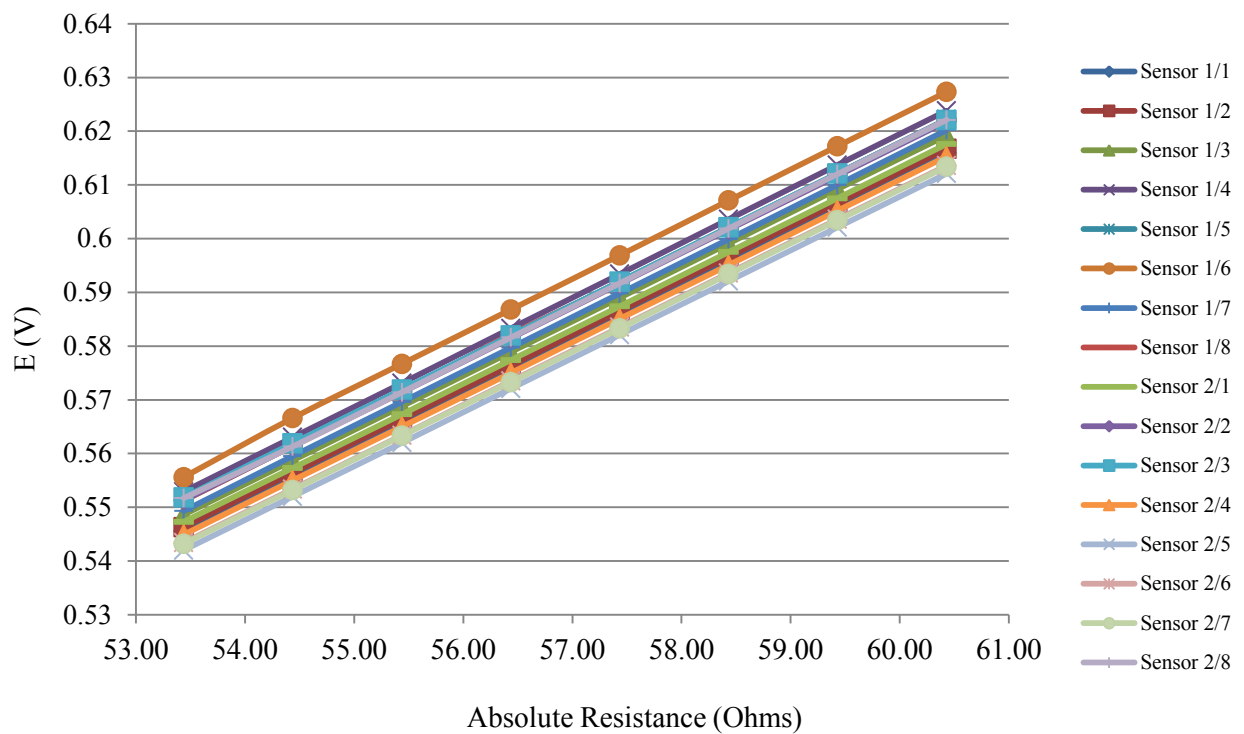


Figure 50: Calibration Curves for Thin Film Elements Operating in Absolute Mode

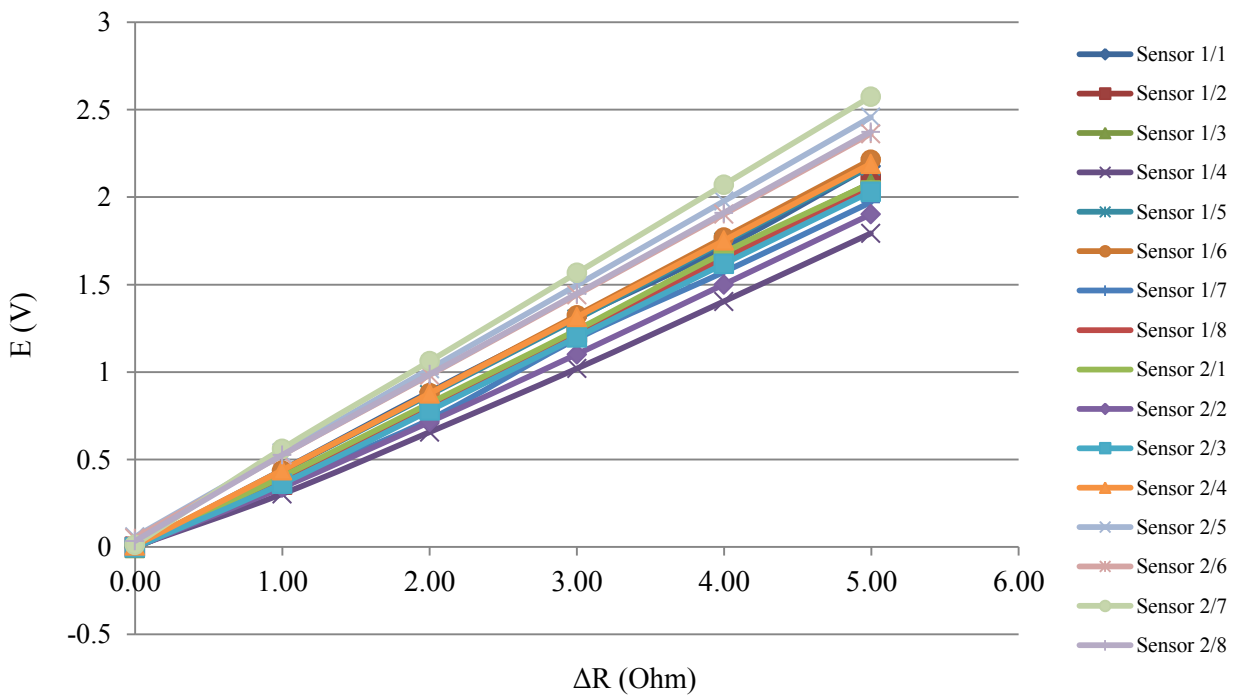


Figure 51: Calibration Curves for Thin Film Elements Operating in Absolute Mode

Gauge	$m \left[\frac{K}{\Omega} \right]$	$\Delta m \left[\frac{K}{\Omega} \right]$	$b [K]$	$\Delta b [K]$	R^2
1/1	6.02868	0.03406	-44.47890	1.48769	0.99994
1/2	6.18482	0.03895	-35.44215	1.61823	0.99992
1/3	6.09771	0.03302	-34.94890	1.38956	0.99994
1/4	5.39018	0.02873	-50.31852	1.42536	0.99994
1/5	5.96912	0.03359	-35.84652	1.44768	0.99994
1/6	5.97726	0.03573	-43.80231	1.57129	0.99993
1/7	6.16602	0.03418	-41.97922	1.44988	0.99994
1/8	5.98366	0.03632	-35.17601	1.55866	0.99993
2/1	6.05168	0.03535	-35.33428	1.50060	0.99993
2/2	6.25472	0.03525	-41.48024	1.47232	0.99994
2/3	5.98767	0.03278	-34.83606	1.40421	0.99994
2/4	6.07250	0.03253	-35.08283	1.37508	0.99994
2/5	5.94439	0.10110	-30.98398	4.31648	0.99942
2/6	6.31466	0.03581	-39.28818	1.47248	0.99994
2/7	6.22693	0.03366	-40.06376	1.40651	0.99994
2/8	6.13714	0.03313	-41.81338	1.41140	0.99994

Table 3: Thin Film Array Calibration in Oven for Both Arrays

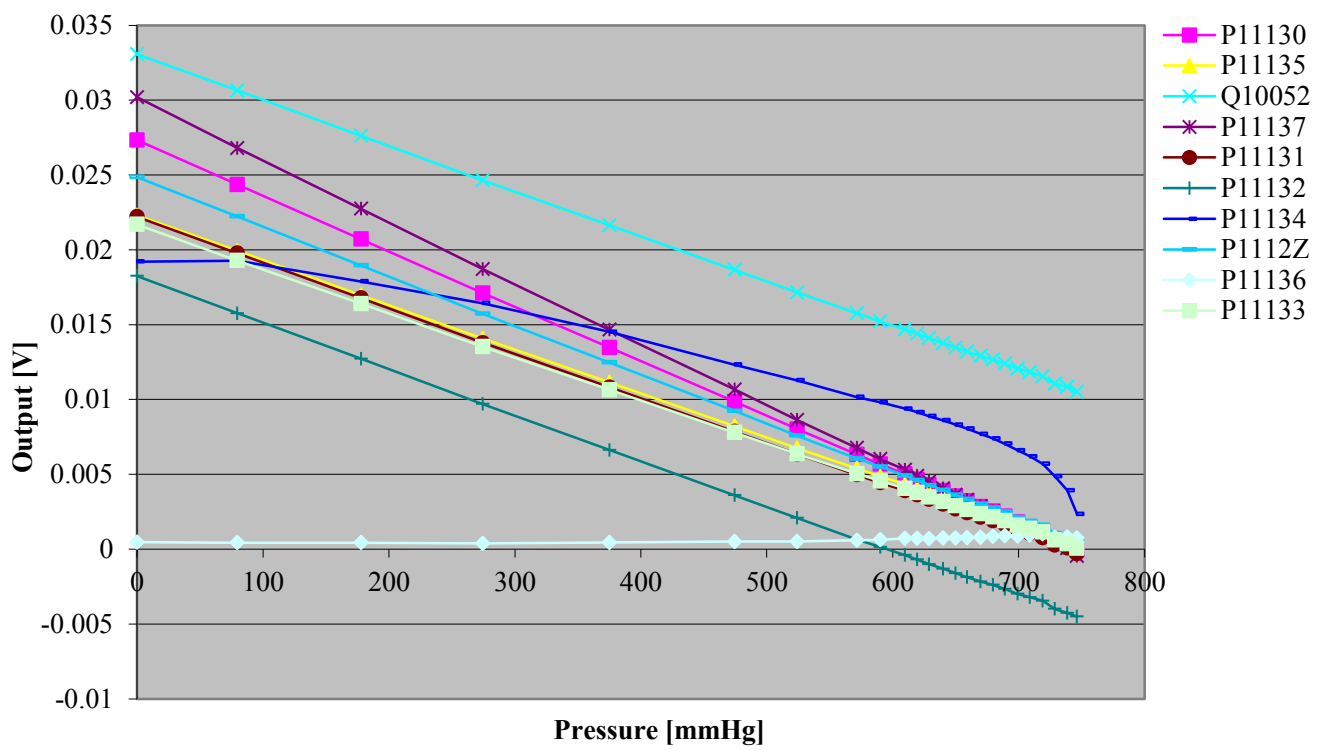


Figure 52: Entrant EPIH-11 Pressure Transducer Calibration Curve

Appendix B – Design Information

GENESIS HIGH SPEED	
GEN SERIES BASIC 1M DIGITIZER	
Specifications	
Basic 1M Digitizer	
Analog Input Sections	
Number of Channels	8
Input Type	single ended metal type BNC, outer shell grounded
Connectors	
Input Ranges	$\pm 1.0\text{ V}$, $\pm 2.0\text{ V}$, $\pm 5.0\text{ V}$, $\pm 10\text{ V}$, $\pm 20\text{ V}$, $\pm 50\text{ V}$, plus variable gain in 1000 steps (0.1 %) 10000 steps (0.1 %)
Offset (zero position)	
Input Coupling	DC, GND, 1MΩ
Impedance	
Maximum Start Error (MSE)	0.1 % full scale
Noise	0.02 % full scale
Analog Bandwidth	500 kHz (-3 dB)
Overload Protection	250 Volt
Number of Shots	4, incl. signal conditions
	6
Acquisition	
Sample Rate	From 1 MS/s to 0.015/s, 16 bit (0.0015 %)
ADC Resolution	
Anti-Alias Filters	Bypass, Time-, Frequency domain optimized
Time Domain	7-pole Bessel 2.50 kHz, optimal step response
Frequency Domain	7-pole Butterworth 4.00 kHz, extended frequency response
Digital Decimation Filters	Off, Frequency domain optimized
Frequency Domain	1.2 pole FIR at sample rate divided by 4, 10, 20, 40
Transient Memory	
Standard	128 MS per card, stored by enabled channels, 8 channels
	16 MS per channel
Triggering	
Each channel has individual dual-level trigger detection with selectable hysteresis, modes and qualifiers.	
Pre- and post-trigger	0 to full memory length
Trigger Rate	Up to 1000 triggers per second, zero re-arm time
Resolution	16 bit for each level (0.0015 %)
Head Office	France
HBM	HBM France SAS 46 rue du Chenevrel, BP 6 95242 Montrésor Cedex Tel: +33 675 873 70 Email: info@fr.hbm.com
Germany	UK
HBM	HBM UK Ltd, Kingdom 1 Churchill Court, 59 Station Road North Harrow, Middlesex, HA1 7AA Tel: +44 1992 633 313 Email: info@uk.hbm.com
Head Office	USA
HBM	HBM Sales Office 29 Bell Street Marlborough, MA 01752, USA Tel: +1 800 523 4653 Email: info@us.hbm.com
PRO Asia	PRO Asia
	HBM Sales Office Room 202B, Jing Guang Center, 19 Bell Street Marlborough, MA 01752, USA Tel: +1 800 523 4653 Email: info@as.hbm.com
HBM Genesis High Speed	HBM Genesis products were previously sold under the Nicolet brand. The Nicolet brand is owned by Thermo Fisher Scientific Inc., Corporation. HBM reserves the right to change this document at any time. It provides outline specification only and cannot be used as the basis of a contract.

Figure 53: Genesis Data Acquisition System Data Sheet

Distribution A: Approved for public release; distribution is unlimited.